Tailoring three-phase microenvironment for high-performance oxygen reduction reaction in PEMFCs

Zipeng Zhao,[1] Md Delowar Hossain,[2,3] Chunchuan Xu,[4] Zijie Lu,[4] Yi-Sheng Liu,[5] Shang-Hsien Hsieh,[6] Ilkeun Lee,[7] Wenpei Gao,[8] Jun Yang,[4] Boris V. Merinov,[2] Wang Xue,[9] Zeyan Liu,[1] Jingxuan Zhou,[1] Zhengtang Luo,[3] Xiaoqing Pan,[8,10] Francisco Zaera,[7] Jinghua Guo,[5,11] Xiangfeng Duan,[9,12] William A. Goddard III,[2] Yu Huang[1, 12]*

[1]Department of Materials Science and Engineering, University of California, Los Angeles, California 90095, United States;

[2]Materials and Process Simulation Center, California Institute of Technology, Pasadena, California 91125, United States;

[3]Department of Chemical and Biological Engineering, The Hong Kong University of Science and Technology, Clear Water Bay, Kowloon 999077, Hong Kong;

[4]Ford Motor Company, Dearborn, Michigan 48121, United States;

[5]The Advanced Light Source, Lawrence Berkeley National Laboratory, Berkeley, California 94720, United States;

[6]National Synchrotron Radiation Research Center (NSRRC), 101 Hsin-Ann Rd., Hsinchu Sci. Park, Hsinchu 30076, Taiwan;

[7]Department of Chemistry and UCR Center for Catalysis, University of California, Riverside, California 92521, United States;

[8]Department of Chemical Engineering and Materials Science, University of California, Irvine, California, 92697, United States;

[9]Department of Chemistry and Biochemistry, University of California, Los Angeles, California 90095, United States;

[10]Department of Physics and Astronomy, University of California, Irvine, Irvine, California 92697, United States;

[11]Department of Chemistry and Chemical Biology, University of California, Santa Cruz, Santa Cruz, California 95064, United States;

[12]California NanoSystems Institute, University of California, Los Angeles, Los Angeles, California 90095, United States

*To whom correspondence should be addressed: yhuang@seas.ucla.edu

Abstract:

Proton exchange membrane fuel cells (PEMFCs) offer an attractive zero-emission mobile power source. However, the requirement of excessive platinum group metal (PGM) catalysts to facilitate the sluggish oxygen reduction reaction (ORR) in PEMFCs has prevented their widespread adoption. Despite tremendous progress in catalyst development with greatly increased catalytic activities, the reduction of PGM loading in practical PEMFCs remains a challenge. The ORR in PEMFCs occurs at a catalyst-electrolyte-gas three-phase interface, with multi-faceted challenges involving the activity of the catalysts, available active sites, and concerted transport of the reactants (oxygen, protons) to and removal of the product (water) from the active sites. The reduction of

PGM loading reduces the number of catalytic sites, requiring a higher reaction rate on each site to sustain the overall power output, which in turn necessitates faster delivery of the reactants to and removal of the products from each active site. A desirable interface must allow efficiently feeding oxygen and protons to the catalytic sites without starving the reaction and must allow timely removal of water to avoid interface flooding. Herein we report the design of the three-phase microenvironment in PEFMCs by tailoring the interactions between the carbon supports and the electrolyte ionomers. We show that the carbon surface with 2.4% oxygen interacts with the ionomers through both its hydrophilic and hydrophobic regions, creating favorable transport paths for rapid delivery of both oxygen and protons, and timely removal of water. Such an elaborated interfacial design allows reducing costly platinum catalysts while maintaining state-of-the-art performance. For the first time we demonstrate PEMFCs with all key ORR catalyst performance metrics, including mass activity, rated power and durability, surpassing the U.S. DOE targets.

Key Words: Three-Phase Interface, Fuel Cell, Oxygen Reduction Reaction, Carbon Engineering

Introduction

Proton exchange membrane fuel cells (PEMFCs) are of immense interest as a zero-emission, quiet mobile power source for automobiles, drones, submarines, and autonomous underwater vehicles[1-3]. Platinum (Pt) group metals (PGMs), particularly Pt, are typically used as the catalysts in commercial PEMFCs, especially as the cathode catalyst for boosting the sluggish oxygen reduction reaction (ORR)[3]. To reduce PGM usage in PEMFCs is essential for lowering the cost to enable more widespread adoption[4,5]. To this end, intensive efforts have been devoted to developing new generations of electrocatalysts with greatly increased mass activities[6-10]. However, such high mass activities are usually only achieved in half-cell rotating disc electrode (RDE) test where the mass transport limitation is compensated using Koutecký–Levich equation, and only represent the fundamental material limit of these new generations of electrocatalysts. To date, the performance advancements achieved in the half-cell RDE test can **hardly** be captured in practical PEMFCs, and the power density target set by the DOE for PEFMCs is rarely met or addressed. Overall, despite tremendous progress in catalyst development, the reduction of PGM loading in practical PEMFCs (*e.g.*, to meet the United States DOE target of cathode loading level ≤ 0.1 mg_{PGM}/cm^2) has met with much less success[5].

The ORR in a practical PEMFC occurs at a *catalyst-electrolyte-gas* three-phase interface. The challenge is multifaceted, involving the activity of catalysts, available active sites, and concerted transport of oxygen and proton through the polymer electrolyte (ionomers) to reach the active sites and the removal of water from the active sites[11]. The reduction of PGM loading reduces the number of catalytic sites and requires a higher reaction rate for each catalytic site to sustain the overall power output, which in turn requires faster delivery of the reactants to and removal of the product from each active site. Therefore, the mass transport resistance starts to play an increasingly limiting role in the electrodes with lower PGM loading[5,12]. To this end, an elaborated *catalyst-electrolyte-gas* three-phase interface design is necessary to facilitate the relevant mass transport processes for efficient ORR. Beyond a highly active and durable Pt-based catalyst[13-17], the gas permeation[18-20], proton conduction[21,22], and water removal[23] are all equally important. Therefore, a desirable three-phase interface must include an efficient ORR catalyst with high intrinsic activity, while simultaneously allowing for **rapidly feeding reactants (O_2 and proton) without starving the reaction and timely removing the product (water) to avoid interface flooding**. This rarely addressed issue is the subject of this study.

Recognizing that the ionomers are mostly in contact with the carbon support, here we focus on chemical modification the carbon support to tailor carbon-ionomer interactions to create a favorable three-phase interface for facilitating the ORR in PEMFCs. Specifically, we used a series of carbon materials with different surface oxygen contents (2.4, 3.8, 12.0%, respectively) as the catalyst support to prepare cathode catalysts in membrane electrode assemblies (MEA) and evaluate their performance. Our systematic studies demonstrate that the catalysts supported on carbon with 2.4% surface oxygen display a state-of-the-art mass activity among all PGM-based (*with PGM as the only active sites*) MEAs reported to date, **for the first time enabling PEMFCs with all key ORR catalyst performance metrics, including mass activity, rated power and durability, exceeding the targets set by the DOE**. Our molecular dynamics (MD) simulations suggest that an optimal surface oxygen ratio on the carbon surface leads to favorable carbon-ionomer interactions[24,25] and a microenvironment comprised of both hydrophobic and hydrophilic paths,[26] which simultaneously allow the efficient shuttle of oxygen molecules and protons to, and timely removal of water from the catalytic sites, providing a desirable microenvironment for highly efficient ORR[27].

Results and Discussion

To explore the impact of surface oxygen in carbon supports on ORR, we prepared catalysts on three types of carbon materials, each with different surface oxygen ratio (labeled as C1, C2, and C3). We employed synchrotron-based near-edge X-ray absorption fine structure (NEXAFS) spectroscopy to determine the ratio of surface oxygen on the surface of each carbon support. The carbon K-edge intensities are comparable for all samples (Fig. 1A), suggesting the identical carbon loading, whereas the oxygen K edge intensity indicates that the oxygen ratio (i.e. oxygen to carbon (O/C) ratio for simplicity of description in this work) qualitatively follows a trend of C1> C2> C3 (Fig. 1B). In addition, components corresponding with C=O, COOH, C-OH vibration modes are identified in both carbon K-edge and oxygen K-edge spectra, suggesting the presence of various oxygen forms on the surface[28-30]. The oxygen-containing surface functional groups are also evidenced by attenuated total reflection (ATR) Fourier-transform infrared spectroscopy (FTIR). The band at ~1750 cm^{-1} can be assigned to C=O, while the band from 1000 to 1300 cm^{-1} can be assigned to C-O. We find that the sum of both intensities follows the trend of C1> C2> C3 (Fig. 1C, full spectra presented in Fig. S1)[31-33]. The quantitative ratio of surface oxygen was obtained via synchrotron-based X-ray photoelectron spectroscopy (XPS). The incident beam energy was fixed at 620 eV, making the inelastic mean free path (IMFP) about 0.6 nm and 1.2 nm for the oxygen 1s and carbon 1s photoelectrons generated, respectively[34]. The surface oxygen ratios were estimated to be 12.0%, 3.8 %, and 2.4 % for C1, C2, and C3, respectively (Fig. 1D-F). Except for the surface oxygen ratio, other key properties of all three carbon materials are comparable. Transmission electron microscopy (TEM) images reveal that C1, C2, and C3 show similar morphology of carbon spheres with an average diameter of 30 nm (Fig. S2A). The N_2 adsorption/desorption tests also reveal similar Brunauer–Emmett–Teller (BET) surface areas in the range of 755-766 m^2/g and comparable pore size distribution for C1, C2, and C3 (Fig. S2B, C, Table S1). X-ray diffraction (XRD) patterns also show identical features, suggesting that these carbon materials share the same layered carbon structure and interplane distance (Fig. S2D, Table S1). However, further decreasing surface oxygen would lead to observable change of pore distribution in the carbon structure (Fig. S3), which would impact mass transport in catalyst layer[18].

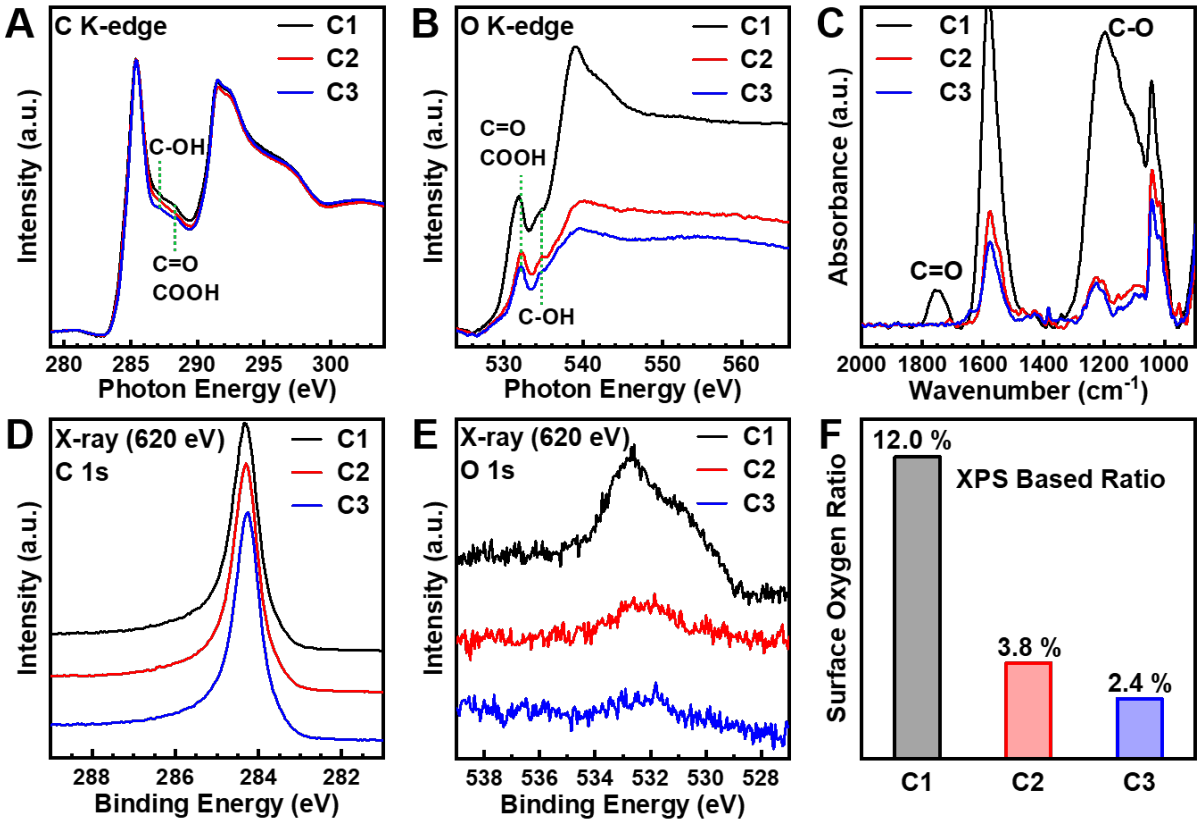

Fig. 1 Characterization of carbon materials. A, B, synchrotron-based NEXAFS spectra for carbon K-edge (A) and for oxygen K-edge (B). The intensity is normalized by sample loading. **c**, ATR-FTIR spectra. **D, E**, synchrotron-based XPS spectra for carbon 1s (D) and oxygen 1s (E). **F**, the surface oxygen to carbon ratio for three carbon samples evaluated; C1, C2, and C3.

To investigate the impact of these carbon supports on fuel cell performance, we prepared PtNi ORR catalysts on these carbons (PtNi/C1, PtNi/C2, PtNi/C3). Specifically, PtNi nanoparticles were directly grown on the respective carbon supports (C1, C2, C3) through a solution-phase synthesis process. They were then annealed in a mixture of Ar and H_2, followed by acid wash and further annealing in Ar and H_2 (details noted in method part). The TEM studies reveal that the PtNi nanoparticles on three different carbon supports exhibit a similar spherical morphology with a comparable average diameter of 4.9-5.0 nm (Fig. S4, 5). The X-ray powder diffraction (XRD) patterns of PtNi/C1, PtNi/C2, and PtNi/C3 are also comparable, which matches well with the comparable Pt ratios (72-74%) revealed by energy dispersive spectroscopy (EDS) (Fig. S5, Table S2). In addition, PtCo/C3 was also synthesized with a similar catalyst size for comparison (Fig. S4, 5, Tables S2). These catalysts were tested by a rotating disk electrode (RDE) system for preliminary ORR performance screening (Fig. S6, Table S3), in which they showed comparable half-cell performance.

The membrane electrode assembly (MEA) was prepared by coating the prepared catalysts directly on the proton exchange membrane as the cathode layer using an ultrasonic spray system. The catalyst coated membrane (CCM), gas diffusion layer (GDL), and gasket were assembled in a fuel cell fixture (details noted in method part). The Pt loading in all prepared MEAs is fixed at 0.10 mg_{PGM}/cm^2 and 0.05 mg_{PGM}/cm^2 for cathode and anode, respectively. The MEAs employed our prepared catalysts showed comparable roughness factor (Table S4). For a fair comparison, all

materials are the same in all prepared MEAs except for the cathode layer catalyst. Thus, the MEAs are labeled by the type of cathode catalysts. All performance metrics in MEA, including ORR mass activity (MA), rated power, and durability, etc. are tested and evaluated following the published DOE guidelines[35].

First, the MA of ORR catalysts in MEA was evaluated by normalizing the iR-free currents at 0.9 V in the H_2/O_2 test by the cathode PGM mass. The beginning of test (BOT) MAs are 0.45, 0.56, 0.62, A/mg_{PGM} for PtNi/C1, PtNi/C2, PtNi/C3, respectively (Fig. 2A, Table S5). It is important to note, although the PtNi nanocatalysts used in these different MEAs showed comparable ORR MA in RDE half-cell test (Fig. S6, Table S3), the ORR MAs observed in MEAs (Fig. 2A) showed notable differences, indicating the mass transport in these MEAs rather than intrinsic catalytic activity plays a dictating role in the overall performance Therefore, the observed trend of MA in PtNi/C1 < PtNi/C2 < PtNi/C3 indicates more efficient mass transport in PtNi/C3 than PtNi/C2 and PtNi/C1. Notably, the beginning of test (BOT) MAs of the PtNi/C1, PtNi/C2, PtNi/C3, PtCo/C3 all surpass the DOE target for MA (0.44 A/mg_{PGM})[35]. Impressively, the MA of PtCo/C3 (0.72 A/mg_{PGM}) is about 2.3 times of the MA (0.32 $A/mg_{PGM,}$) of the benchmark Tanaka Kikinzoku Kogyo (TKK) Pt/C and represents the state-of-the-art MA for PGM-based ORR catalysts achieved in MEA tests to date (Table S5).

The durability of the MEA performance is critical for long term stable operation of practical PEMFCs. To test the practical durability of MEA performance with reasonable experimental time in a laboratory setting, the US DOE has recently suggested a standard accelerated durability test (ADT) protocol, in which a square wave potential between 0.60 and 0.95 V (3-s hold at each voltage) is applied to the MEA for 30,000 cycles with a targeted end of test (EOT) MA above 60% of BOT MA, and a minimum value above 0.26 A/mg_{PGM}. Although an ADT protocol with a triangle wave between 0.60 and 1.0 V (50 mV/s sweep rate) was commonly used in previous studies, the newly suggested square wave protocol shows five times acceleration factor over the triangle wave protocol and is proven to be much harsher than triangle wave protocol to better reflect the long-term durability of the MEA in practical devices[36]. **Notably, PtNi/C3, PtCo/C3 MEAs all retain more than 60% of initial MA (DOE target) after 30000 cycles square wave ADT[35], and with EOT MA exceeding the DOE target.** To the best of our knowledge, this represents the first time that the MEA durability and EOT performance exceeds the DOE target after the suggested square wave ADT, highlighting the long-term durability of our MEAs for practical PEMFCs[37].

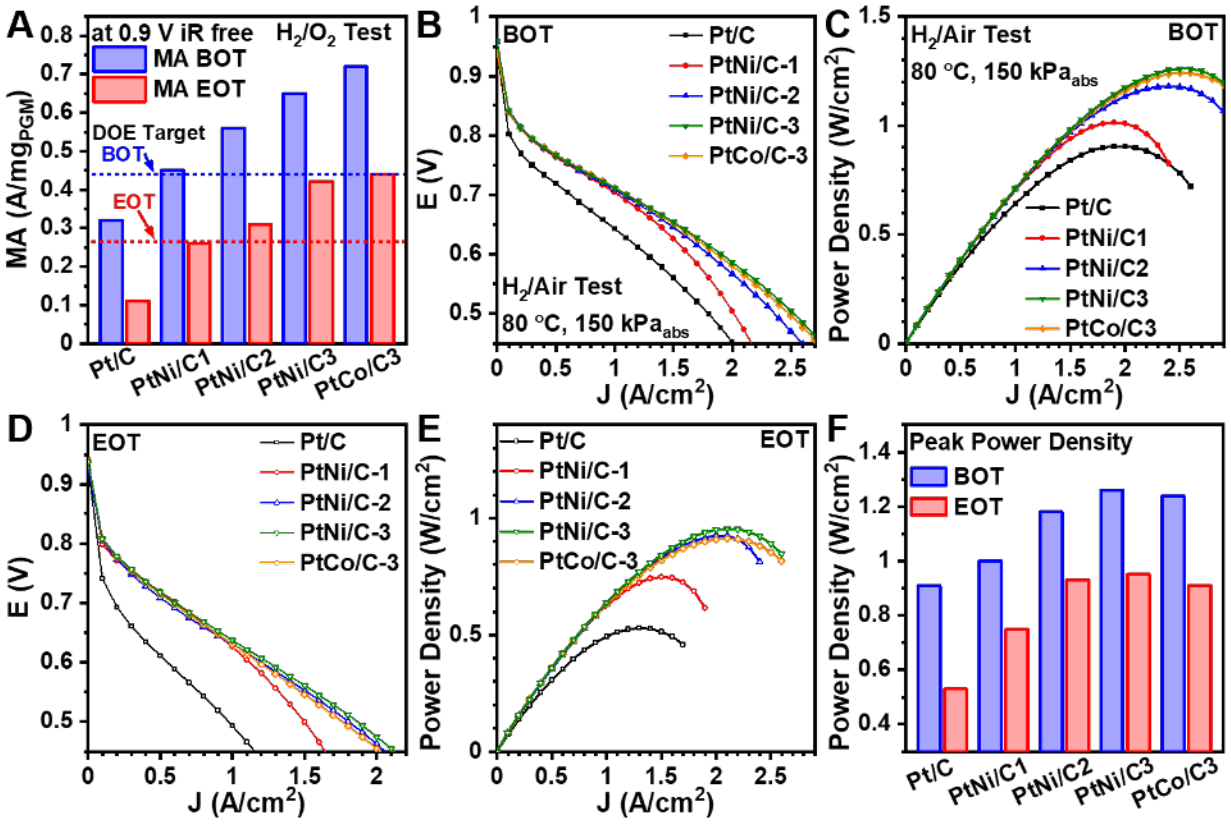

Fig. 2 Membrane electrode assembly (MEA) test. A, Comparison of mass activities obtained in the H_2/O_2 test at the beginning of test (BOT; before ADT) and end of test (EOT; after ADT). **B-E**, H_2/Air test. **B**, polarization plots at BOT. **C**, power densities plots at BOT. **D**, polarization plots at EOT. **E**, power densities plots at EOT. **F**, Comparison of peak power densities. The MEA test was performed at 80 ºC and 150 kPa_{abs} pressure unless specifically noted.

To further evaluate the performance of these MEAs in fuel cell working environment, we next obtained the current/power polarization plot using air as an oxygen source (Fig. 2B, C). It was observed at low current densities, all our catalysts perform rather similarly and show higher performance than Pt/C. At higher current density where mass transport starts to play an increasingly important role, the differences start to show up for C1, C2, C3 supported catalysts: a much obvious voltage drop was observed in PtNi/C1 while PtNi/C2, PtNi/C3, and PtCo/C3 better maintained their performance in this mass-transport region (Fig. 2B). Such differences can be more clearly seen in the power density plots (Fig. 2C). Power density values, especially at high current densities, are good indicators for PEMFC performance related to the mass transports, including proton, oxygen transport, and water removal. The peak power densities of the prepared MEAs follow the trend of PtNi/C1<PtNi/C2 < PtNi/C3 ≈ PtCo/C3 (Fig. 2C, F) which is similar to the trend of MAs (Fig. 2A), again supporting that mass transport is more efficient in C3-based catalyst layer than that of C2-based and much more than C1-based. Thus**, the performance differences observed in both H_2/O_2 and H_2/Air tests can all be attributed to the different mass transport limitations related to the different carbon supports used.** We have further characterized the EOT performance following the aggressive square wave ADT protocol suggested by DOE to evaluate the durability of the MEAs. At the EOT, all MEAs based on our catalysts are significantly better than that using Pt/C (Fig. 2D, E). Compared to BOT, the peak power density follows the

same trend of PtNi/C1<PtNi/C2<PtNi/C3, though the difference between PtNi/C3 and PtNi/C2 is smaller (Fig. 2E, F, Fig.S7).

Furthermore, we have also evaluated the rated power of the MEAs. The rated power of an MEA takes into account of heat rejection, which is an important aspect during practical fuel cell operation as the mass transport induced power loss at high current density is converted to waste heat. Thus, the DOE sets a target of $Q/\Delta T$ <1.45 kW/°C for heat rejection, which translates to the targeted rated power > 1 W/cm^2 measured at 0.67 V when working temperature is 94 °C[18,35,38] (see Methods for details). Thus, the rated power is an important figure of merit directly reflecting the performance of practical fuel cells at working conditions, which is, however, rarely reported. **Significantly, our PtNi/C3 and PtCo/C3 MEAs deliver a rated power of 1.21 and 1.16 W/cm^2, respectively, both above the DOE target (1W/cm^2) (Fig. 3). Furthermore, the EOT rated power of both PtNi/C3 (1.05 W/cm^2) and PtCo/C3 (1.03 W/cm^2) remained above the DOE target after the square wave ADT (Fig. 3B)[35], showing significant promise for long term stable operation.** It is important to note that the rated power corresponds directly to the working performance of practical PEMFCs. The achievement of rated power target both before and after ADT clearly highlights the practical potential of our MEAs.

The voltage loss at a fixed current density from the BOT to EOT is another important measure characterizing the durability of the PEMFC operation. Significantly, the **voltage losses for the PtNi/C3 and PtCo/C3 MEAs at 0.8 A/cm^2 after the square wave ADT is only 16.2 and 16.9 mV, respectively, far below the U.S. DOE target (< 30 mV)** (Fig. 3C)[35]. These evaluations attest the superior performance, especially the sustained high MEA performance after ADT, of these designed catalysts compared to previously reported catalysts (Table S6)[18,39]. Although our studies have focused only on the catalyst layer, there are excellent examples in the literature to improve MEA rated power by optimizing membrane, ionomer, gas diffusion layer, or gas flow pattern design[40-42]. For instance, we expect further enhancement may be achieved if the state-of-the-art Gore ultrathin membrane is used [43].

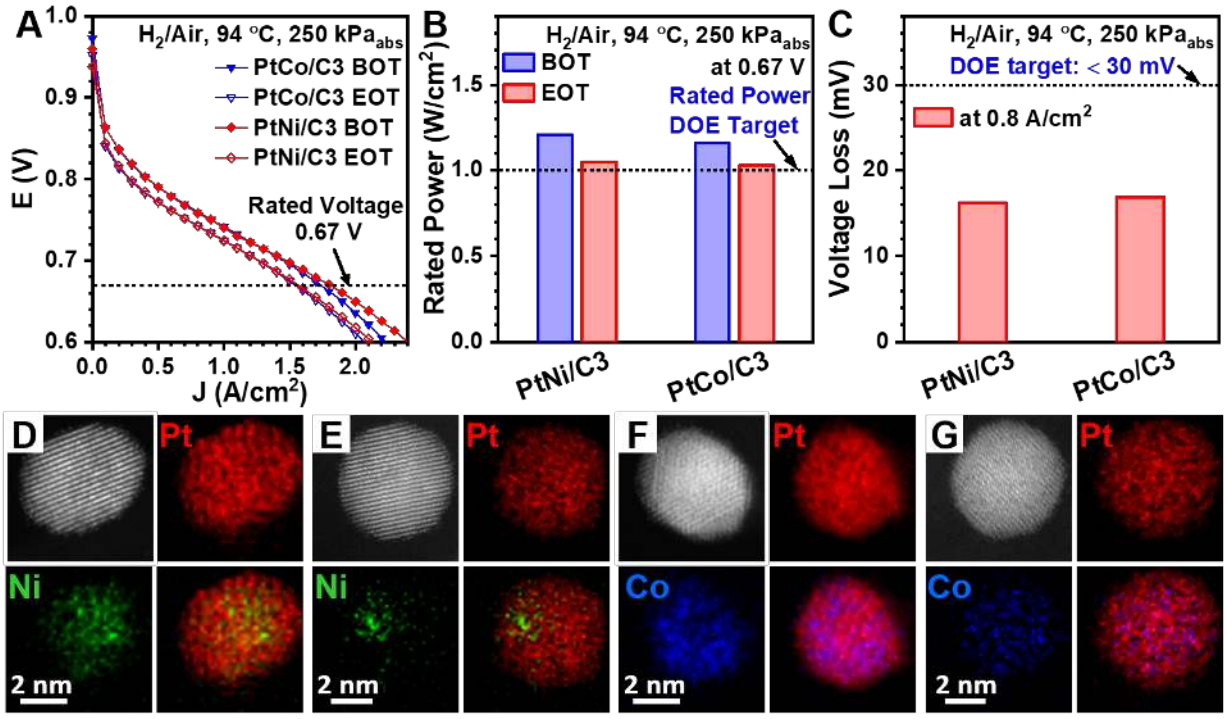

Fig. 3 Rated power of representative MEAs and EDS map analysis of cathode catalysts. A, H_2/Air polarization plots obtained at the temperature of 94 ºC and pressure of 250 KPa_{abs} for rated power evaluation. **B**, Comparison of rated power densities at BOT and EOT in for PtNi/C3, PtCo/C3. **C,** Voltage loss from BOT to EOT at a fixed current density of 0.80A/cm^2. **D-G,** STEM image and EDS elemental analysis of representative Pt-based nanoparticles. PtNi/C3 samples before MEA test (**D**), at EOT **(E).** PtCo/C3 samples before MEA test (**F**), and at EOT (**G**). Each panel consists of the STEM image, mapping image of individual elements, and combined mapping of both elements.

Furthermore, we performed TEM, scanning transmission electron microscopy (STEM), and EDS analysis on catalysts at EOT. The Pt/C exhibited significant size coarsening, with average size increasing from 3.8 ± 1.1 nm (before the test) to 6.3 ± 1.5 nm (EOT, after ADT), which can explain the 66% MA loss in H_2/O_2 test and the large voltage loss in the H_2/Air test (Fig. 2, Fig. S8, Table S5). We also observed size coarsening in TEM images for the Pt-alloy nanocatalysts, but to a much less degree. The sizes of the original PtNi nanocatalysts prepared on C1, C2, C3 are 4.9 ± 1.0 nm, 4.9 ± 1.0 nm, 4.9 ± 1.1 nm, respectively, while the sizes of the corresponding PtNi nanoparticles after ADT are 6.1 ± 1.7 nm, 6.1 ± 1.6 nm, 6.1 ± 1.6 nm, respectively (Fig. S4). The size of PtCo nanoparticles grown on C3 is 5.0 ± 0.7 nm (before test and), and 6.0 ± 1.5 nm at EOT (Fig. S4). The coarsening of nanocatalysts leads to a decrease in surface active sites, which contributes to the observed performance degradation at EOT.

In addition, we also observed a loss of non-noble transition metal in the evaluated catalysts at EOT. The atomic ratio of Ni drops from 28.1% to 11.2%, 26.7% to 10.8%, 25.8% to 10.4% for PtNi/C1, PtNi/C2, PtNi/C3, respectively. The atomic ratio of Co decreases from 17.9% to 10.7% for PtCo/C3 (Table S2). More interestingly, these nanocatalysts demonstrated excellent structural durability, as revealed in EDS elemental maps. The representative PtNi catalyst demonstrates a Pt-rich shell structure (Fig. 3D), which has been suggested to be important for high durability in Pt alloy nanocatalysts[44]. The Pt-rich shell was retained at EOT but with increased thickness, as

evidenced by the EDS map (Fig. 3E). Compared to the PtNi with a more concentrated Ni distribution in the core region, PtCo shares a similar core-shell structure with a Pt-rich shell, but Co is more dispersed in the PtCo nanocatalysts both before the MEA test and at EOT. The loss of Ni, Co is indicated by a comparison of the relative intensity change of Ni, Co in the EDS maps (Fig. 3D-F). It is noted that the leached metal cations may also poison the ionomers and also contribute to the performance degradation after ADT (Fig. 2D-F)[45].

It is recognized that the three-phase interface is critical for MEA performance[18]. However, due to the complexity of the interface and lack of reliable characterization techniques, there is little atomic-scale insight on the three-phase interface, especially the ionomer/substrate interface. For instance, the electron-beam based techniques suffer from beam-induced damage on ionomer[46,47]. Soft X-ray based low radiation damage techniques provide the best resolution at sub-15 nm scale, which is far from the resolution needed for capturing the nanometer scale feature of the ionomer structure and distribution at the three-phase interface[46,48]. Therefore, we performed molecular dynamics (MD) simulation to investigate the effect of the surface oxygen ratio in carbon support on the interaction between the support and the perfluorosulfonic acid (PFSA) ionomers at the atomic scale. We also studied the impact of the above interactions on fuel cell performance.

To build the carbon support model, we equilibrated the amorphous carbon portion in the model using Reactive Force Field (ReaxFF) based molecular dynamics calculations (using LAMMPS) (Fig. S9A). Then, we added three top layers of graphitic carbon on the top of pre-equilibrated amorphous carbon to simulate the surface structure of carbon, as noted in the literature[49,50]. This core-shell carbon model leads to a predicted density of 2.15 g/cm^3, with a predicted X-ray diffraction pattern with the (002) peak at 26° and (100) peaks at 42° diffraction angle, which are in good agreement with experimental observation (Fig. 1, Fig. S9B). Then, the top graphitic surface was oxidized at four different surface oxygen ratios (0%, 2.5%, 4.0%, and 12.0%) with the distribution of C=O, C-OH, and COOH oxygenated functional groups based on experimental results. These sites are evidenced by corresponding bonds detected in NEXAFS (Fig. 1A, B)[28,30]. Then, we equilibrated the predicted structure for 100 ps at 300 K (Fig. S10) using ReaxFF reaction dynamics.

To describe the electrolyte, we used hydrated PFSA ionomers and equilibrated at 600 K for 200 ps. The PFSA ionomer includes two portions, the polar or hydrophilic portion composed of sulfonic groups ($-SO_3^-$), and the non-polar or hydrophobic PTFE backbone. To determine the interaction between the PFSA ionomers and the carbon surface, we used ReaxFF MD to equilibrate the hydrated PFSA ionomer structures on top of four different carbon surfaces at 300K for 200 ps and then predicted their interaction energy (Fig. S11)[42]. The carbon surface with 2.5% oxygen shows stronger interaction compared to other carbon surfaces (0%, 4.0% or 12.0% oxygen) (Fig. 4A, Table S7). It is also noted that the carbon with 2.5% surface oxygen demonstrates the largest number of ionomer atoms within 0.3 nm distance from the carbon surface, which reflects the interface energy since those atoms contribute to the bonding between the ionomers and the carbon surface (Fig. 4B). The stronger interaction between the hydrated PFSA ionomers and carbon surface (2.5% oxygen) leads to a more uniform distribution of the ionomers, which in turn alleviates the known mass transfer issue in the catalyst layer due to uneven distribution of the ionomers[24,25]. Indeed, the PtNi/C3 (C3 contains 2.4% surface oxygen) MEA displays the smallest pressure independent oxygen transport resistance ($R^{P\text{-}ind}$) (Fig. 4D, Fig. S12).

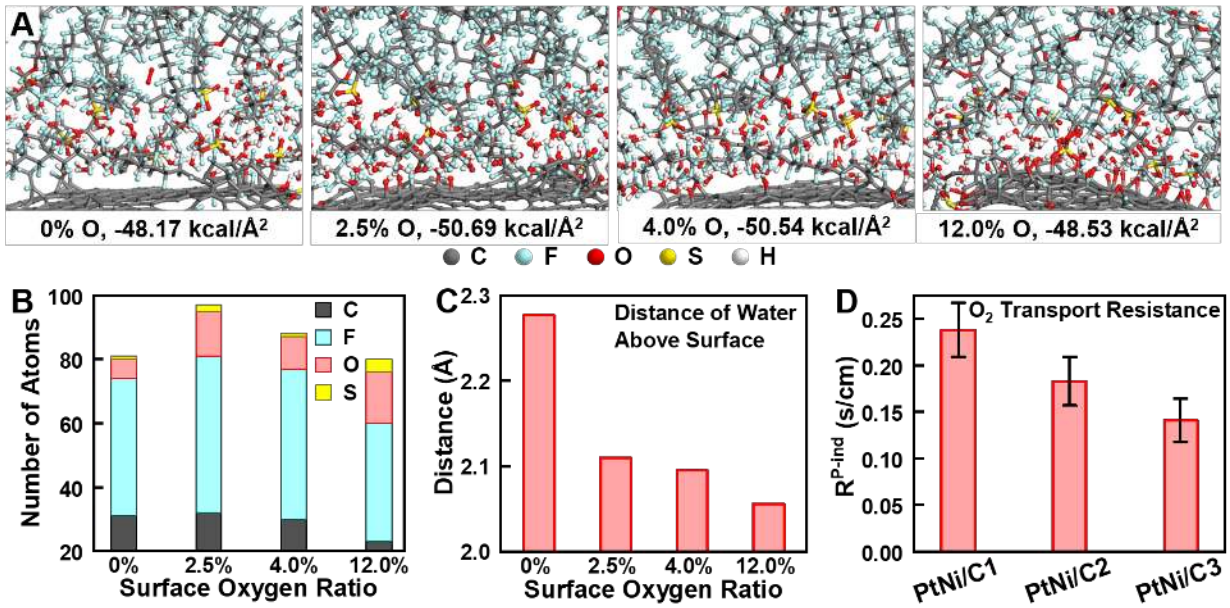

Fig. 4 The interfacial interactions between the carbon surface and hydrated PFSA ionomers. A, The image of ionomer, water distribution on carbon surfaces after MD simulation. The bottom caption shows interface energy between the ionomers and the carbon surface with different oxygen contents (0%, 2.5%, 4.0 %, and 12.0%). **B**, The number of atoms belongs to the ionomer distributed within 0.3 nm distance above carbon surfaces in simulation models (model size: 3.4 nm in width, 3.4 nm in depth). **C**, The average distance of water molecules within 0.3 nm above carbon surfaces. **D**, Pressure independent parts of oxygen transport resistance measured at 80 °C, RH 65% (details noted in Method part). Error bars represent standard error.

Additionally, our simulation shows that the water molecules are repelled further away from the carbon surface as the surface oxygen ratio decreases, as indicated by the average distance of water molecules above the carbon surface (within 0.3 nm) (Fig. 4C). Thus, the simulation suggests that the carbon with lower surface oxygen ratio may have a lesser problem of interface water flooding in MEA (Fig. 4C), which can help explain the better durability of PtNi/C3 compared to PtNi/C2, PtNi/C1 since excess water and flooding can accelerate the electrode degradation[23]. The calculated results show that the carbon surface with 0% oxygen interacts only with the hydrophobic PTFE part of the PFSA ionomer (via C-F and C-C interactions) (Fig. 4A). In contrast, the 12.0% oxygenated surface is highly hydrophilic and allows only the sulfonic group to bind on its highly oxygenated surface, with very few non-polar groups on the carbon sites (Fig. 4A). In contrast, 2.5% and 4.0% oxygenated surfaces have both hydrophilic (sulfonic-oxygenated carbon) and hydrophobic (C-F, C-C) interactions within the interface (Fig. 4A). Together, the C3 shows strongest interactions with both hydrophilic and hydrophobic parts of the ionomers, which simultaneously promotes both O_2 and proton transfer: i.e., O_2 prefers a hydrophobic region (PTFE backbone) and diffuses through it quickly while the proton (H_3O^+) and water prefer hydrophilic part (sulfonic acid side chain) for fast diffusion[51]. Thus the most desirable three-phase interface should involve a combination of both the hydrophilic and hydrophobic interface near or next the catalysts facilitating O_{ad}, OH_{ad}, and H_2O_{ad} formation[27].

Conclusion

Together, this work demonstrates that carbon surface chemistry plays a critical role in the MEA performance of Pt-based catalysts in practical PEMFCs. We showed that the Pt alloy nanocatalysts

on carbon support with an optimal surface oxygen ratio lead to state-of-the-art MEA performance, with all the key ORR performance metrics including mass activities, rated power, and durability, exceeding DOE targets (Table 1). We attribute this outstanding performance to the favorable interaction between the carbon substrate and the ionomers, which results in a more uniform distribution of ionomers in the catalyst layer and a desirable microenvironment involving both hydrophilic and hydrophobic paths that facilitate the balanced supply of protons and oxygen molecules to the catalytic sites, as well as the timely removal of water molecules from the interface. These findings highlight the critical role of the three-phase microenvironments in facilitating catalytic reactions in a complex system, and opens a new pathway to greatly boost the performance of practical PEMFCs.

Table 1. Summary of DOE technical targets and the performance achieved in our MEAs with a tailored three-phase microenvironment. The cathode loading is maintained at 0.10 mg_{PGM}/cm^2 for all MEAs.

Performance Metrics	Unit	DOE Target	PtNi/C3	PtCo/C3
Mass Activity	A/mg_{PGM} @0.9V iR free	>0.44	0.65	0.72
Loss in Mass Activity (EOT vs. BOT)	%	<40%	35%	39%
Rated Power	W/cm^2	>1.00	1.21	1.16
Loss in voltage at 0.8 A/cm^2 (EOT vs. BOT)	mV	<30.0	16.2	16.9

Experimental Procedures

Chemicals and Materials

Platinum (II) acetylacetonate [$Pt(acac)_2$], nickel(II) acetylacetonate [$Ni(acac)_2$], nickel(II) acetate tetrahydrate [$Ni(Ac)_2{\cdot}4H_2O$], cobalt (II) acetate tetrahydrate [$Co(Ac)_2{\cdot}H_2O$], benzyl acid (BA), Nafion dispersion, Aquivion D83-06A ionomer dispersion were purchased from Sigma Aldrich. Bis(triphenylphosphine)dicarbonylnickel [$(C_6H_5)_3P]_2Ni(CO)_2$) was purchased from Alfa Aesar. N, N-Dimethylformamide (DMF), acetone, isopropanol (IPA) were purchased from Fisher Scientific. Ethanol was purchased from Decon Labs, Inc. SGL-29BC gas diffusion layer (GDL), polytetrafluoroethylene (PTFE) gasket were purchased from The Fuel Cell Store. Carbon black (Ketjenblack EC-300J) was obtained from Fitz Chem LLC. Water used was Ultrapure Millipore (18.2 MΩ·cm).

Preparation of Carbon Materials (C1, C2, C3, C4)

C1 was prepared by annealing Ketjenblack EC-300J in the air at 400˚C to achieve increased oxygen ratio on carbon surface. C2 was the original Ketjenblack EC-300J. C3-C4 were prepared by annealing Ketjenblack EC-300J in a gas mixture of argon (Ar) and hydrogen (H_2) at 800˚C-1000˚C for to achieve reduced surface oxygen ratio.

Synthesis of PtNi/C (C can be either C1, C2, C3)

1. Solution phase synthesis

140 mg carbon black (C1, C2, or C3) and 28 mg $[(C_6H_5)_3P]_2Ni(CO)_2$ were dispersed in 135 mL DMF under ultrasonication for 30 mins in a 325 mL pressure bottle (sealed). 190 mg $Pt(acac)_2$, 110 mg $Ni(ac)_2 \cdot 4H_2O$, and 1030 mg benzoic acid were dissolved in 25 ml DMF in a 20 mL vial. Then the prepared solution noted above was added into the 325 ml pressure bottle and mixed with carbon black and $[(C_6H_5)_3P]_2Ni(CO)_2$ solution. After ultrasonication for 5 mins, the sealed pressure bottle was directly put into 140 ºC oil bath and then slowly heated to 160 ºC. The pressure bottle was then kept at 160 ºC for 48 hrs (hrs). After reaction finished, the catalyst was collected by centrifugation, then dispersed and washed with isopropanol and acetone mixture. The centrifugation and re-dispersion steps were repeated for three times. Then the catalysts were dried in vacuum at room temperature.

2. Pre-Acid Wash Annealing

The dried catalyst was then annealed at 250 ºC for 2 hrs in Ar and H_2 mixture (the volume ratio of Ar/H_2 =500/1).

3. Acid Wash

About 200 mg of annealed catalyst is dispersed in 20 ml 0.2 M H_2SO_4 in a 25 mL vial. The dispersion was then purged with N_2 till N_2 saturation. Then the vial is kept in 85 ºC for 6 hrs. The catalyst was collected through centrifugation when the acid wash is finished, then dispersed and washed with water. The centrifugation and re-dispersion steps were repeated for three times. Then the catalysts were dried in vacuum at room temperature.

4. Post-Acid Wash Annealing

The dried catalyst was then annealed at 200 ºC for 2 hrs in Ar and H_2 mixture (the volume ratio of Ar/H_2 =500/1).

Synthesis of PtCo/C3

1. Solution phase synthesis

140 mg carbon black (C3) was dispersed in 135 mL DMF under ultrasonication for 30 mins in a 325 mL pressure bottle (sealed). 190 mg $Pt(acac)_2$, 140 mg $Co(ac)_2 \cdot 4H_2O$, and 1030 mg benzoic acid were dissolved in 25 ml DMF in a 20 mL vial. Then the prepared solution noted above was added into the 325 ml pressure bottle and mixed with carbon black solution. After ultrasonication for 5 mins, the sealed pressure bottle was directly put into 140 ºC oil bath and then slowly heated to 160 ºC. The pressure bottle was then kept at 160 ºC for 48 hrs. After reaction finished, the catalyst was collected by centrifugation, then dispersed and washed with isopropanol and acetone mixture. The centrifugation and re-dispersion steps were repeated for three times. Then the catalysts were dried in vacuum at room temperature.

2. Pre-Acid Wash Annealing

The dried catalyst was then annealed at 400 ºC for 2 hrs in Ar and H_2 mixture (the volume ratio of Ar/H_2 =500/1).

3. Acid Wash

About 200 mg of annealed catalyst was dispersed in 20 ml 0.2 M H_2SO_4 in a 25 mL vial. The dispersion was then purged with N_2 till N_2 saturation. Then the vial is kept in 85 ºC for 6 hrs. The

catalyst was collected through centrifugation when the acid wash is finished, then dispersed and washed with water. The centrifugation and re-dispersion steps were repeated for three times. Then the catalysts were dried in vacuum at room temperature.

4. Post-Acid Wash Annealing

The dried catalyst was then annealed at 200 ºC for 2 hrs in Ar and H_2 mixture (the volume ratio of Ar/H_2 =500/1).

Characterization

Transmission electron microscopy (TEM) images were taken with an FEI T12 transmission electron microscope operated at 120 kV. Atomic resolution high angle annular dark-field (HAADF) images, as well as energy-dispersive spectroscopy (EDS) maps, were taken using a JEOL Grand ARM300CF scanning/transmission electron microscopy (S/TEM) operated at 300 kV. HAADF images were also taken using an FEI TITAN operated at 200 kV at STEM mode. The TEM/STEM sample grids were prepared by dispersing the sample in a mixture of water and ethanol, then dripping the dispersion onto carbon-coated aluminum grids (Ted Pella, Redding, CA) using a pipette and drying under ambient condition. X-ray powder diffraction (XRD) patterns were collected with a Panalytical X'Pert Pro X-ray Powder Diffractometer with Cu-Kα radiation. The concentration of catalysts was determined by inductively coupled plasma atomic emission spectroscopy (ICP-AES, Shimadzu ICPE-9000) as well as by EDS coupled in FEI TITAN TEM. The data for the Brunauer–Emmett–Teller (BET) surface areas and pore distributions were acquired with a Micromeritics Tristar II 3020 surface area and porosity analyzer. ATR-FTIR spectra were recorded by using a horizontal reflection ATR accessory (PIKE Technology, MIRacle, ZnSe crystal) and a DTGS detector coupled to an FTIR spectrometer (Bruker, Tensor 27). The spectra were the result of averaging data from 1024 scans, taken with a 4 cm^{-1} resolution. The synchrotron radiation based high-resolution XPS measurements were carried out at Taiwan Light Source beamline 09A1 of National Synchrotron Radiation Research Center (NSRRC), Taiwan. The measurements were conducted at room temperature. The photon energy for XPS measurements was set at 620 eV. The photon energies were calibrated by the Au 4f core level signal emitted from a clean gold foil electrically connected with the samples. The intensities were normalized by photoionization cross-section of each element for comparing the surface oxygen to carbon ratio. The near-edge X-ray absorption fine structure (NEXAFS) spectroscopy measurements on Carbon and Oxygen K-edge were carried out on beamline 7.3.1 at the Advanced Light Source, Lawrence Berkeley National Laboratory, CA. The energy resolution on Carbon and Oxygen K-edge was set to 0.2 eV and recorded in total electron yield mode with careful energy calibration before and after the experiment.

Electrode Preparation and Electrochemistry Test

A typical catalyst ink was prepared by mixing 2 mg of catalyst powder (PtNi/C1, PtNi/C2, PtNi/C3, PtCo/C3) with 2 mL of ethanol solution containing 16 µL of Nafion (5 wt%) with 5 min ultrasonication time. The benchmark Pt/C ink was prepared by mixing 1.5 mg of Pt/C powder with 2 mL of ethanol solution containing 20 µL of Nafion (5 wt%) with 5 min ultrasonication time. Then, 10 µL of prepared ink was dropped onto a 5 mm diameter glassy carbon electrode (Pine Research Instrumentation). Estimation of platinum group metal (PGM) loading was based on the overall PGM ratio within catalyst determined by ICP-AES. The ink was dried under an infrared lamp. Then the electrode was ready for the electrochemical test.

A three-electrode cell was used to carry out the electrochemical measurements. The working electrode was a catalyst coated glassy carbon electrode. An Ag/AgCl electrode was used as the reference electrode. Pt wire was used as the counter electrode. Cyclic Voltammetry (CV) measurements were conducted in an N_2 saturated 0.1 M $HClO_4$ solution between 0.05 to 1.1 V vs. reversible hydrogen electrode (RHE) at a sweep rate of 100 mV/s. Electrochemical active surface area (ECSA) was measured by integrating the hydrogen underpotential deposition (H_{upd}) peak in CV, assuming 210 $\mu C/cm^2_{PGM}$. Oxygen reduction reaction (ORR) measurements were conducted in an O_2 saturated 0.1 M $HClO_4$ solution between 0.05 to 1.05 V vs. RHE at a sweep rate of 20 mV/s. Accelerated durability test (ADT) was performed in an oxygen saturated 0.1 M $HClO_4$ solution by applying square wave potential sweeps between 0.6 to 0.95 V vs. RHE (0.6 V 3s and 0.95 V 3s) for 30000 cycles.

Membrane Electrode Assemblies (MEA) Fabrication and Test

A series of catalysts were investigated as the cathode catalyst layers in MEA testing. The catalyst inks were made by mixing the catalysts with the ionomer solution (Aquivion D83-06A) and water-IPA solvent mixture, followed by sonicating the dispersion in ice water for 1.5 hrs. The fresh inks were then spray-coated onto the Johnson Matthey (JM) half catalyst-coated membrane (CCM) by using a Sono-Tek ultrasonic spray system. The anode catalyst layer on the JM half-CCM had a platinum loading of 0.05 $mg_{PGM}\ cm^{-2,}$ and the membrane thickness was 18 µm. The cathode catalyst loading was controlled to be 0.10 $mg_{PGM}\ cm^{-2}$, which was confirmed by the ICP measurements. The fabricated CCM was dried in a vacuum oven to evaporate the solvents completely. Two 3-mil PTFE sheets were pressed to make a gasket (total thickness: 6 mil). A gas diffusion layer (GDL), which includes a microporous layer, was used (total thickness 230 µm). Two GDLs, two gaskets, and the prepared CCM were pressed to make the MEA. Then, MEAs were loaded in Fuel Cell Technology 5 cm^2 single-cell hardware and tested in the Scribner 850e fuel cell test stand under 80 °C, 150 kPa_{abs} (abs: absolute; all pressure noted in this work refer to the absolute pressure) and 100% relative humidity (RH), following the U.S. Department of Energy (DOE) fuel cell test protocol. The gas flow rate was 1500/2000 sccm during H_2/Air and H_2/O_2 test for anode/cathode, respectively. The ADT for Pt-based catalysts was performed using a square wave voltage from 0.6 V to 0.95 V with a duration of 3 seconds for each voltage level, according to the U.S. DOE MEA ADT protocol for PGM based catalysts. Each test was run up to 30,000 cycles at 80 °C, 150 kPa_{abs}, 100% RH with H_2/N_2 flow 100/100 sccm for anode and cathode, respectively. The MEA's beginning of test (BOT) and end of test (EOT) performance metrics, such as polarization curves, MA, ECSA, high-frequency resistance (HFR) by alternating current (AC) impedance and H_2 crossover, were recorded by the Scribner 850e fuel cell test station and the Scribner 885 potentiostat associated with the 850e fuel cell station. The ECSA was determined by integrating the hydrogen underpotential deposition (H_{upd}) peak in CV, assuming 210 $\mu C/cm^2_{PGM}$. The H_2/O_2 and H_2/Air BOT performance represented the average test results of at least two fabricated MEAs.

Rated Power Test for MEA

MEAs employing PtNi/C3 or PtCo/C3 as a cathode catalyst were prepared in a similar way as noted above. The BOT rated power of prepared MEA was tested in Scribner 850e fuel cell test stand under 94 °C, 250 $kPa_{abs,}$ and 100% RH. We chose the testing condition of 94 °C for better comparison with a representative previous work[18]. The H_2/Air gas flow rate was 835/2000 sccm for anode/cathode, respectively. Then, the durability test, which involves 30,000 cycles of square wave (0.6 V maintained 3s, 0.95 V maintained 3s) at 150 kPa_{abs}, 80 °C, was performed for the

tested MEA. The H_2/N_2 gas (100% RH) flow was 100/100 sccm for anode and cathode, respectively. Then EOT rated power of the MEA was tested under 94 °C, 250 $kPa_{abs,}$ and 100% RH. The H_2/Air gas (100% RH) flow rate was 835/2000 sccm for anode/cathode, respectively.

The U.S. DOE assumes 90 kW stack gross power (P_{stack}) required for 80 kW net power and sets a heat rejection target, $Q/\Delta T_i$ of <1.45. The rated power was measured at rated voltage (V_{rated}), which can be defined by the following equation 1 (Eq. 1) [35].

$$\frac{Q}{\Delta T_i} = \frac{P_{stack}(1.25 - V_{rated})}{V_{rated}(T_{stack} - T_{ambient})} \quad \text{Eq. 1}$$

The U.S. DOE protocol assumes P_{stack} = 90 kW and $T_{ambient}$ =40 °C, if T_{stack} =94 °C, $Q/\Delta T_i$ =1.445, which meets the target ($Q/\Delta T_i$ of ≤1.45), the V_{rated} will be around 0.67 V. Thus, the rated power will be measured at 0.67 V.

Oxygen Transport Resistance Test for MEA

The MEA was tested at 80 °C with 65% RH for both anode and cathode. Ultrahigh pure hydrogen was applied in the anode. The mix-gas of O_2 and N_2 was pre-mixed by Airgas, Inc., and the mix-gas cylinders were used as a gas source. The dry O_2 mole ratios for pre-mixed gases were 0.981%, 1.491%, and 2.001%, which was determined by Airgas, Inc. In order to identify the pressure independent part of the total oxygen transport resistance, the test was performed at a total pressure of 110, 150, 190, 230, and 270 kPa_{abs}. The total oxygen transport resistance can be approximately obtained by the following Eq. 2.

$$R_{total} = \frac{4FC_{O_2}}{i_{lim}} = \frac{4F}{i_{lim}} \times \frac{P_{abs} - P_{H_2O}}{RT} \times x_{O_2-dry} \quad \text{Eq. 2}$$

$R_{total}^{O_2}$ presents the total oxygen transport resistance. C_{O_2} represents oxygen concentration. P_{abs} is the total pressure. P_{H_2O} is the pressure of water vapor at testing temperature. x_{O_2-dry} is the dry O_2 ratio. i_{lim} represents the limit current density.

The limit current density was identified as the largest current density (considering the absolute value) obtained through linear voltage sweep (0.12 to 0.41 V, 2 mV/s) using the 885 potentiostat attached to the 850e fuel cell station. The total oxygen transport resistance can be separated into pressure dependent part ($R^{P\text{-}d}$) and pressure independent part ($R^{P\text{-}ind}$), which represents the Knudsen diffusion and diffusion of oxygen through the ionomer layer [52,53]. The relationship of total oxygen resistance (R_{total}), pressure dependent part of oxygen transport resistance ($R^{P\text{-}d}$), and pressure independent part of oxygen transport resistance ($R^{P\text{-}ind}$) can be expressed in the following Eq. 3.

$$R_{total} = R^{P-d} + R^{P-ind} \quad \text{Eq. 3}$$

Computational details

The calculations were performed by using Reactive Force Field (ReaxFF) implemented in the molecular dynamics package LAMMPS [54,55], which differs from traditional unreactive force fields by

- Describing the electrostatic interactions using a distributed atom size charge on each atom that was allowed to change on every step of MD, allowing the electrostatic to change as reactions occur.
- Allowing all valence interactions to break, going to zero at large separations

- Describing the bond breaking using a bond distance dependent bond order and a bond order dependent bond energy.

- Including electrostatic and van der Waals interactions between all atoms (even bonded ones) since the valence bonds can break. Since the charges were distributed over the size of the atoms, Coulombic interactions were shielded, going to a constant at short distances (point charges lead to infinities)

Thus, during MD simulations of reactive systems, many bonds may form or break.

All ReaxFF MD simulations were performed with 0.2 fs time step to allow charges and bonds to be described properly as bonds were broken and formed.

We used 2.15 g/cm^3 carbon density in a three-dimensional (3D) periodic MD simulation box consisting of around 3000 carbon atoms. This system was melted by heating to 6000 K for 5 ps and ten quenched to 300 K over 5.7 ps (1000 K/ps), followed by equilibrated at 300K for 100 ps to obtain amorphous carbon. Then we introduced 3 graphitic layers top of the amorphous carbon, heated to 3500 K for 100 ps for equilibration, and quenched again to 300K at 100 K/ps rate.

The surface layer was oxidized with 0%, 2.5%, 4.0%, and 12.0% oxygen to carbon ratio to simulate experimental observation. Here we used the ratios of functionalized C from experimental results. The hydrated ionomer was heated and equilibrated at 600 K for 100 ps and then cooled down and further equilibrated at 300 K for 100 ps. Then the hydrated PFSA ionomer was placed on the top of the carbon surfaces having different oxidized graphitic surfaces and equilibrated for 200 ps at 300K (12 H_2O/sulfonic acid [-SO_3^-] at ionomer and carbon interface).

The interaction between hydrated perfluorosulfonic acid (PFSA) ionomer (based on the molecular structure of Nafion from previous simulations [51]) and the carbon surface was calculated via energy minimization and equilibration. The interface energies were calculated by using the Eq. 4.

$$\text{Interface energy (kcal/area)} = \frac{(E_{Total}(carbon+Nafion) - E_{carbon}(carbon\ subs.) - E_{Nafion}(Nafion))}{Interace\ area} \quad \text{Eq. 4}$$

Supplementary Information

Supplementary information is available for this paper online.

Acknowledgments

Y.H., X.D., W.A.G., Z.Z., M.D.H., B.M., W.X., and Z.L. acknowledge support from the Office of Naval Research by the grant number of N00014-18-1-2155. Y.H., Z.Z. Z.L. also acknowledge the Defense University Research Instrumentation Program (DURIP) support by the grant number of N000141812271. I. L. and F. Z. acknowledge financial support from the U. S. National Science Foundation, Division of Chemistry, under grant number CHE-1854439. W.A.G. thanks NSF (CBET-1805022) for partial support. The authors thank the Chemical Engineering & Fuel Cell Department of Ford Motor Company for assistance in MEA preparation and testing. This research used resources of the Advanced Light Source, which is a DOE Office of Science User Facility under contract no. DE-AC02-05CH11231. The authors thank the National Synchrotron Radiation Research Center (NSRRC) scientists for their skillful assistance during the synchrotron radiation

XPS measurement. EDS mapping on JEM Grand ARM was conducted using the facilities in the Irvine Materials Research Institute (IMRI) at the University of California Irvine.

Author Contributions

Z.Z. and Y.H. conceived the idea and designed the experiments. Z.Z. conducted the materials preparation, characterization, fuel cell test at UCLA. W.X. Z. L. J.Z. contributed to the experiments at UCLA. M.D.H., B.M. conducted the MD simulations while Z.L., W.A.G. supervised the simulations. C.X. Z.L. J.Y. conducted the fuel cell test in Ford. Y.L. conducted synchrotron-based NEXAFS experiment, and J.G. supervised the experiment. S.H. performed the synchrotron-based XPS test. I.L. conducted the ATR-FTIR test, and F.Z. supervised the work. W.G. conducted the EDS mapping analysis, and X.P. supervised the work. Z.Z., X.D., Y.H. wrote the paper with substantial input from other authors. Y.H. supervised the whole project.

Declaration of Interests

A U.S. provisional patent, "High performance platinum-based catalyst combined with carbon support engineering" (application No. 62/905,564), has been filed by UCLA. The processing conditions and related characterization results of the carbon materials have been submitted for a patent application. The rest of the data and figures in this work have not been presented or published elsewhere.

Data Statement

All data needed to evaluate our conclusions are found in the main text and the Supplementary Information. Further data related to the paper are available from the corresponding authors on reasonable request.

Reference

1 Weydahl, H., Gilljam, M., Lian, T., Johannessen, T. C., Holm, S. I. & Hasvold, J. Ø. (2019). Fuel cell systems for long-endurance autonomous underwater vehicles – challenges and benefits. Int. J. Hydrogen Energy,

2 Ustolin, F. & Taccani, R. (2018). Fuel cells for airborne usage: Energy storage comparison. Int. J. Hydrogen Energy 43, 11853-11861.

3 Debe, M. K. (2012). Electrocatalyst approaches and challenges for automotive fuel cells. Nature 486, 43.

4 Kongkanand, A., Gu, W. & Mathias, M. F.(2017). in *Encyclopedia of Sustainability Science and Technology* (ed Robert A. Meyers) 1-20 (Springer New York).

5 Kongkanand, A. & Mathias, M. F. (2016). The Priority and Challenge of High-Power Performance of Low-Platinum Proton-Exchange Membrane Fuel Cells. J. Phys. Chem. Lett. 7, 1127-1137.

6 Seh, Z. W., Kibsgaard, J., Dickens, C. F., Chorkendorff, I., Nørskov, J. K. & Jaramillo, T. F. (2017). Combining theory and experiment in electrocatalysis: Insights into materials design. Science 355, eaad4998.

7 Pedersen, C. M., Escudero-Escribano, M., Velázquez-Palenzuela, A., Christensen, L. H., Chorkendorff, I. & Stephens, I. E. L. (2015). Benchmarking Pt-based electrocatalysts for low temperature fuel cell reactions with the rotating disk electrode: oxygen reduction and hydrogen oxidation in the presence of CO (review article). Electrochim. Acta 179, 647-657.

8 Xie, C., Niu, Z., Kim, D., Li, M. & Yang, P. (2020). Surface and Interface Control in Nanoparticle Catalysis. Chem. Rev. 120, 1184-1249.

9 Jacob, T. & Goddard III, W. A. (2006). Water Formation on Pt and Pt-based Alloys: A Theoretical Description of a Catalytic Reaction. ChemPhysChem 7, 992-1005.

10 Zhang, Z., Luo, Z., Chen, B., Wei, C., Zhao, J., Chen, J., Zhang, X., Lai, Z., Fan, Z., Tan, C. *et al.* (2016). One-Pot Synthesis of Highly Anisotropic Five-Fold-Twinned PtCu Nanoframes Used as a Bifunctional Electrocatalyst for Oxygen Reduction and Methanol Oxidation. Adv. Mater. 28, 8712-8717.

11 Holdcroft, S. (2014). Fuel Cell Catalyst Layers: A Polymer Science Perspective. Chem. Mater. 26, 381-393.

12 Weber, A. Z. & Kusoglu, A. (2014). Unexplained transport resistances for low-loaded fuel-cell catalyst layers. J. Mater. Chem. A 2, 17207-17211.

13 Li, W., Chen, Z., Xu, L. & Yan, Y. (2010). A solution-phase synthesis method to highly active Pt-Co/C electrocatalysts for proton exchange membrane fuel cell. J. Power Sources 195, 2534-2540.

14 Han, B., Carlton, C. E., Kongkanand, A., Kukreja, R. S., Theobald, B. R., Gan, L., O'Malley, R., Strasser, P., Wagner, F. T. & Shao-Horn, Y. (2015). Record activity and stability of dealloyed bimetallic catalysts for proton exchange membrane fuel cells. Energy Environ. Sci. 8, 258-266.

15 Jia, Q., Caldwell, K., Strickland, K., Ziegelbauer, J. M., Liu, Z., Yu, Z., Ramaker, D. E. & Mukerjee, S. (2015). Improved Oxygen Reduction Activity and Durability of Dealloyed PtCox Catalysts for Proton Exchange Membrane Fuel Cells: Strain, Ligand, and Particle Size Effects. ACS Catal. 5, 176-186.

16 Li, J., Xi, Z., Pan, Y.-T., Spendelow, J. S., Duchesne, P. N., Su, D., Li, Q., Yu, C., Yin, Z., Shen, B. *et al.* (2018). Fe Stabilization by Intermetallic L10-FePt and Pt Catalysis Enhancement in L10-FePt/Pt Nanoparticles for Efficient Oxygen Reduction Reaction in Fuel Cells. J. Am. Chem. Soc. 140, 2926-2932.

17 Li, J., Sharma, S., Liu, X., Pan, Y.-T., Spendelow, J. S., Chi, M., Jia, Y., Zhang, P., Cullen, D. A., Xi, Z. *et al.* (2019). Hard-Magnet L10-CoPt Nanoparticles Advance Fuel Cell Catalysis. Joule 3, 124-135.

18 Yarlagadda, V., Carpenter, M. K., Moylan, T. E., Kukreja, R. S., Koestner, R., Gu, W., Thompson, L. & Kongkanand, A. (2018). Boosting Fuel Cell Performance with Accessible Carbon Mesopores. ACS Energy. Lett. 3, 618-621.

19 Inoue, G. & Kawase, M. (2016). Effect of porous structure of catalyst layer on effective oxygen diffusion coefficient in polymer electrolyte fuel cell. J. Power Sources 327, 1-10.

20 Nonoyama, N., Okazaki, S., Weber, A. Z., Ikogi, Y. & Yoshida, T. (2011). Analysis of Oxygen-Transport Diffusion Resistance in Proton-Exchange-Membrane Fuel Cells. J. Electrochem. Soc. 158, B416-B423.

21 Kreuer, K. D., Schuster, M., Obliers, B., Diat, O., Traub, U., Fuchs, A., Klock, U., Paddison, S. J. & Maier, J. (2008). Short-side-chain proton conducting perfluorosulfonic acid ionomers: Why they perform better in PEM fuel cells. J. Power Sources 178, 499-509.

22 Yu, H., Roller, J. M., Mustain, W. E. & Maric, R. (2015). Influence of the ionomer/carbon ratio for low-Pt loading catalyst layer prepared by reactive spray deposition technology. J. Power Sources 283, 84-94.

23 Li, H., Tang, Y., Wang, Z., Shi, Z., Wu, S., Song, D., Zhang, J., Fatih, K., Zhang, J., Wang, H. *et al.* (2008). A review of water flooding issues in the proton exchange membrane fuel cell. J. Power Sources 178, 103-117.

24 Orfanidi, A., Madkikar, P., El-Sayed, H. A., Harzer, G. S., Kratky, T. & Gasteiger, H. A. (2017). The Key to High Performance Low Pt Loaded Electrodes. J. Electrochem. Soc. 164, F418-F426.

25 Ott, S., Orfanidi, A., Schmies, H., Anke, B., Nong, H. N., Hübner, J., Gernert, U., Gliech, M., Lerch, M. & Strasser, P. (2019). Ionomer distribution control in porous carbon-supported catalyst layers for high-power and low Pt-loaded proton exchange membrane fuel cells. Nat. Mater. 19, 77-85.

26 Jang, S. S., Molinero, V., Çağın, T. & Goddard, W. A. (2004). Nanophase-Segregation and Transport in Nafion 117 from Molecular Dynamics Simulations: Effect of Monomeric Sequence. J. Phys. Chem. B 108, 3149-3157.

27 Sha, Y., Yu, T. H., Merinov, B. V., Shirvanian, P. & Goddard, W. A. (2011). Oxygen Hydration Mechanism for the Oxygen Reduction Reaction at Pt and Pd Fuel Cell Catalysts. J. Phys. Chem. Lett. 2, 572-576.

28 Zhang, L., Ji, L., Glans, P.-A., Zhang, Y., Zhu, J. & Guo, J. (2012). Electronic structure and chemical bonding of a graphene oxide–sulfur nanocomposite for use in superior performance lithium–sulfur cells. Phys. Chem. Chem. Phys. 14, 13670-13675.

29 Banerjee, S., Hemraj-Benny, T., Balasubramanian, M., Fischer, D. A., Misewich, J. A. & Wong, S. S. (2004). Ozonized single-walled carbon nanotubes investigated using NEXAFS spectroscopy. Chem. Commun., 772-773.

30 Banerjee, S., Hemraj-Benny, T., Balasubramanian, M., Fischer, D. A., Misewich, J. A. & Wong, S. S. (2004). Surface Chemistry and Structure of Purified, Ozonized, Multiwalled Carbon Nanotubes Probed by NEXAFS and Vibrational Spectroscopies. ChemPhysChem 5, 1416-1422.

31 Wang, W., Ruiz, I., Lee, I., Zaera, F., Ozkan, M. & Ozkan, C. S. (2015). Improved functionality of graphene and carbon nanotube hybrid foam architecture by UV-ozone treatment. Nanoscale 7, 7045-7050.

32 O'Reilly, J. M. & Mosher, R. A. (1983). Functional groups in carbon black by FTIR spectroscopy. Carbon 21, 47-51.

33 Prest, W. M. & Mosher, R. A.(1982). in *Colloids and Surfaces in Reprographic Technology* Vol. 200 *ACS Symposium Series* Ch. 11, 225-247 (AMERICAN CHEMICAL SOCIETY).

34 Powell, C. J. & Jablonski, A.(2010). NIST Electron Inelastic-Mean-Free-Path Database - Version 1.2. (National Institute of Standards and Technology).

35 *Fuel Cell Technologies Office Multi-Year Research, Development, and Demonstration Plan*, <https://www.energy.gov/eere/fuelcells/downloads/fuel-cell-technologies-office-multi-year-research-development-and-22> (2017).

36 Stariha, S., Macauley, N., Sneed, B. T., Langlois, D., More, K. L., Mukundan, R. & Borup, R. L. (2018). Recent Advances in Catalyst Accelerated Stress Tests for Polymer Electrolyte Membrane Fuel Cells. J. Electrochem. Soc. 165, F492-F501.

37 Borup, R. L., Kusoglu, A., Neyerlin, K. C., Mukundan, R., Ahluwalia, R. K., Cullen, D. A., More, K. L., Weber, A. Z. & Myers, D. J. (2020). Recent developments in catalyst-related PEM fuel cell durability. Current Opinion in Electrochemistry 21, 192-200.

38 *DOE Technical Targets for Polymer Electrolyte Membrane Fuel Cell Components*, <https://energy.gov/eere/fuelcells/doe-technical-targets-polymer-electrolyte-membrane-fuel-cell-components> (2016).

39 Zhao, Z., Chen, C., Liu, Z., Huang, J., Wu, M., Liu, H., Li, Y. & Huang, Y. (2019). Pt-Based Nanocrystal for Electrocatalytic Oxygen Reduction. Adv. Mater. 31, 1808115.

40 Yoshida, T. & Kojima, K. (2015). Toyota MIRAI Fuel Cell Vehicle and Progress Toward a Future Hydrogen Society. Electrochem. Soc. Interface. 24, 45-49.

41 Ozden, A., Shahgaldi, S., Li, X. & Hamdullahpur, F. (2019). A review of gas diffusion layers for proton exchange membrane fuel cells—With a focus on characteristics, characterization techniques, materials and designs. Prog. Energy Combust. Sci. 74, 50-102.

42 Kusoglu, A. & Weber, A. Z. (2017). New Insights into Perfluorinated Sulfonic-Acid Ionomers. Chem. Rev. 117, 987-1104.

43 Kienitz, B., Kolde, J., Priester, S., Baczkowski, C. & Crum, M. (2011). Ultra-Thin Reinforced Ionomer Membranes to Meet Next Generation Fuel Cell Targets. ECS Trans. 41, 1521-1530.

44 Cao, L., Zhao, Z., Liu, Z., Gao, W., Dai, S., Gha, J., Xue, W., Sun, H., Duan, X., Pan, X. *et al.* (2019). Differential Surface Elemental Distribution Leads to Significantly Enhanced Stability of PtNi-Based ORR Catalysts. Matter 1, 1567-1580.

45 Sulek, M., Adams, J., Kaberline, S., Ricketts, M. & Waldecker, J. R. (2011). In situ metal ion contamination and the effects on proton exchange membrane fuel cell performance. J. Power Sources 196, 8967-8972.

46 G. A. Melo, L., Hitchcock, A. P., Jankovic, J., Stumper, J., Susac, D. & Berejnov, V. (2017). Quantitative Mapping of Ionomer in Catalyst Layers by Electron and X-ray Spectromicroscopy. ECS Trans. 80, 275-282.

47 Cullen, D. A., Koestner, R., Kukreja, R. S., Liu, Z. Y., Minko, S., Trotsenko, O., Tokarev, A., Guetaz, L., Meyer, H. M., Parish, C. M. *et al.* (2014). Imaging and Microanalysis of Thin Ionomer Layers by Scanning Transmission Electron Microscopy. J. Electrochem. Soc. 161, F1111-F1117.

48 Wu, J., Zhu, X., West, M. M., Tyliszczak, T., Shiu, H.-W., Shapiro, D., Berejnov, V., Susac, D., Stumper, J. & Hitchcock, A. P. (2018). High-Resolution Imaging of Polymer Electrolyte Membrane Fuel Cell Cathode Layers by Soft X-ray Spectro-Ptychography. J. Phys. Chem. C 122, 11709-11719.

49 Soboleva, T., Zhao, X., Malek, K., Xie, Z., Navessin, T. & Holdcroft, S. (2010). On the Micro-, Meso-, and Macroporous Structures of Polymer Electrolyte Membrane Fuel Cell Catalyst Layers. ACS Appl. Mater. Interfaces 2, 375-384.

50 Yu, P. T., Gu, W., Makharia, R., Wagner, F. T. & Gasteiger, H. A. (2006). The Impact of Carbon Stability on PEM Fuel Cell Startup and Shutdown Voltage Degradation. ECS Trans. 3, 797-809.

51 Goddard, W., Merinov, B., van Duin, A., Jacob, T., Blanco, M., Molinero, V., Jang, S. S. & Jang, Y. H. (2006). Multi-paradigm multi-scale simulations for fuel cell catalysts and membranes. Mol. Simulat. 32, 251-268.

52 Baker, D. R., Caulk, D. A., Neyerlin, K. C. & Murphy, M. W. (2009). Measurement of Oxygen Transport Resistance in PEM Fuel Cells by Limiting Current Methods. J. Electrochem. Soc. 156, B991-B1003.

53 Garsany, Y., Atkinson, R. W., Gould, B. D. & Swider-Lyons, K. E. (2018). High power, Low-Pt membrane electrode assemblies for proton exchange membrane fuel cells. J. Power Sources 408, 38-45.

54 van Duin, A. C. T., Dasgupta, S., Lorant, F. & Goddard, W. A. (2001). ReaxFF: A Reactive Force Field for Hydrocarbons. J. Phys. Chem. A 105, 9396-9409.

55 Plimpton, S. (1995). Fast Parallel Algorithms for Short-Range Molecular Dynamics. J. Comput. Phys. 117, 1-19.

56 Kongkanand, A., Subramanian, N. P., Yu, Y., Liu, Z., Igarashi, H. & Muller, D. A. (2016). Achieving High-Power PEM Fuel Cell Performance with an Ultralow-Pt-Content Core–Shell Catalyst. ACS Catal. 6, 1578-1583.

Supplementary Information

Tailoring three-phase microenvironment for high-performance oxygen reduction reaction in PEMFCs

This supporting file includes:

Fig. S1 to S12

Table S1 to S7

The sequence is the same as they are mentioned in the main text.

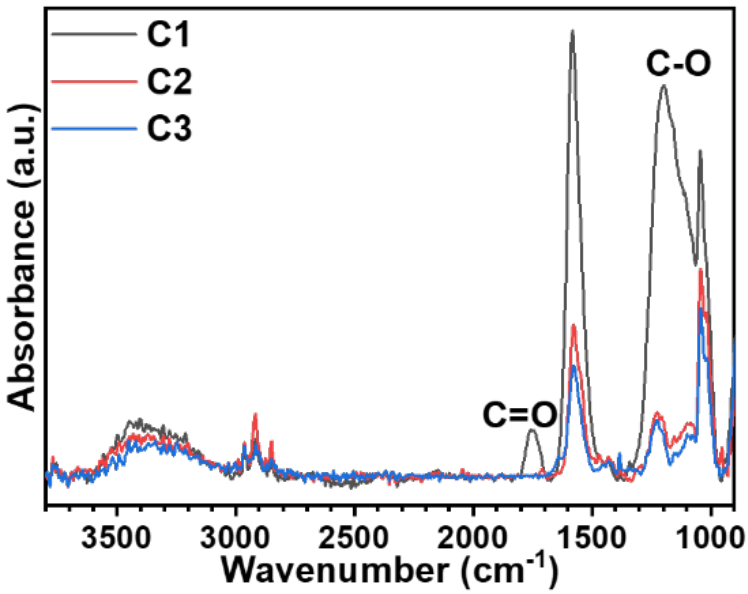

Fig. S1. ATR-FTIR spectra of our three carbon materials with surface oxygens.

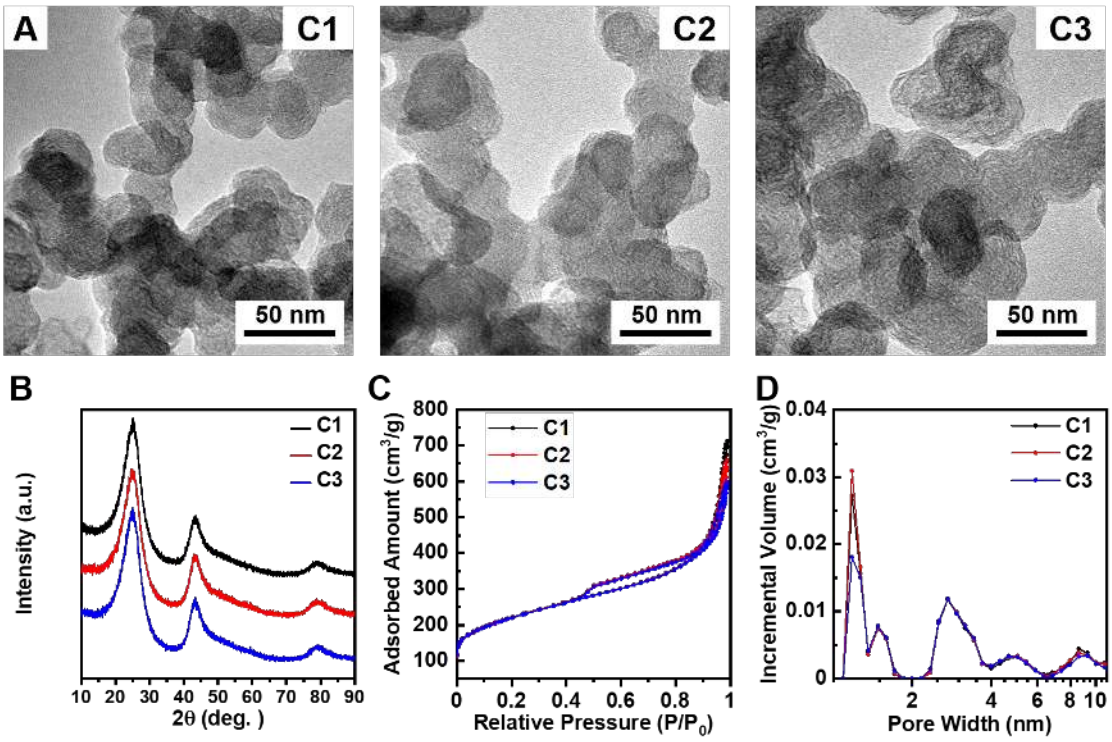

Fig. S2. Characterization of carbon materials. **(A)** TEM images, **(B)** XRD spectra, **(C)** N2 adsorption-desorption isothermal plots, **(D)** pore size distribution calculated from density function theory (DFT) model using nitrogen isothermal plots in **(C)**.

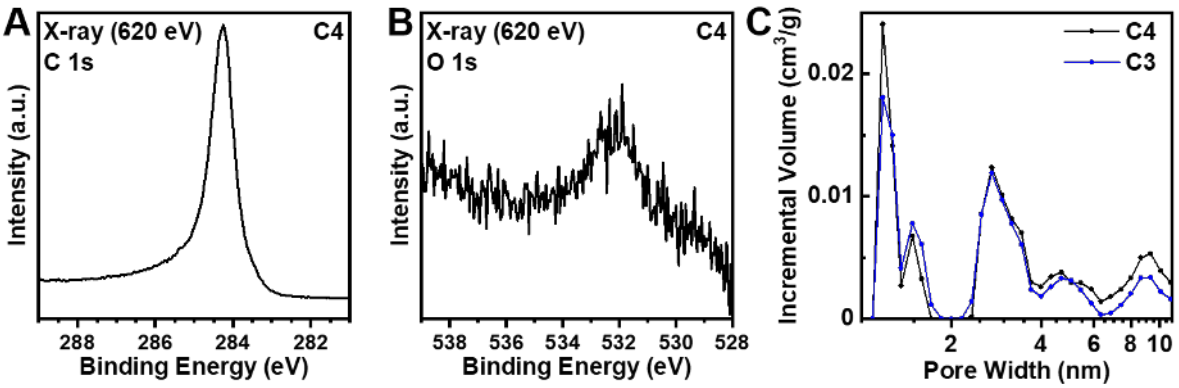

Fig. S3. Spectra of C4 in synchrotron based XPS: **(A)** C 1s, **(B)** O 1s. The estimated surface oxygen to carbon ratio is 1.4%. **(C)** Pore size distribution calculated from density function theory (DFT) model based on N2 isothermal adsorption-desorption test.

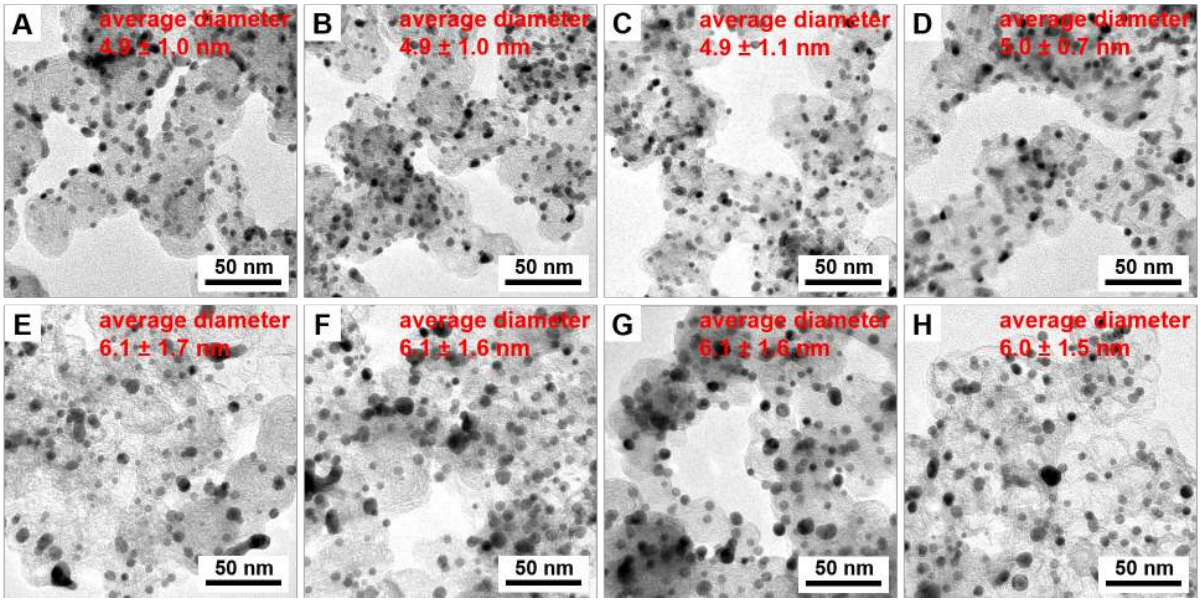

Fig. S4. TEM images of catalysts. Catalysts before MEA test: **(A)** PtNi/C1, **(B)** PtNi/C2, **(C)** PtNi/C3, **(D)** PtCo/C3. Catalysts after 30k square wave cycles in MEA test: **(E)** PtNi/C1, (**F)** PtNi/C2, **(G)** PtNi/C3, **(H)** PtCo/C3.

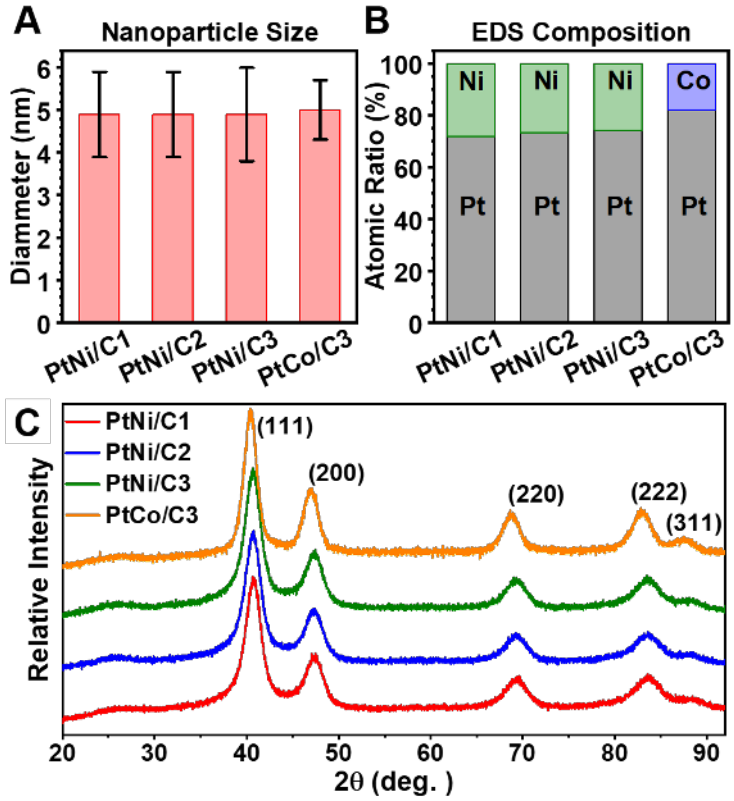

Fig. S5. Characterization of prepared catalysts. (A) The diameter of nanoparticles based on TEM images in **Fig. S3**.The error bar represents standard deviation. **(B)** EDS composition. **(C)** XRD spectra of prepared catalysts.

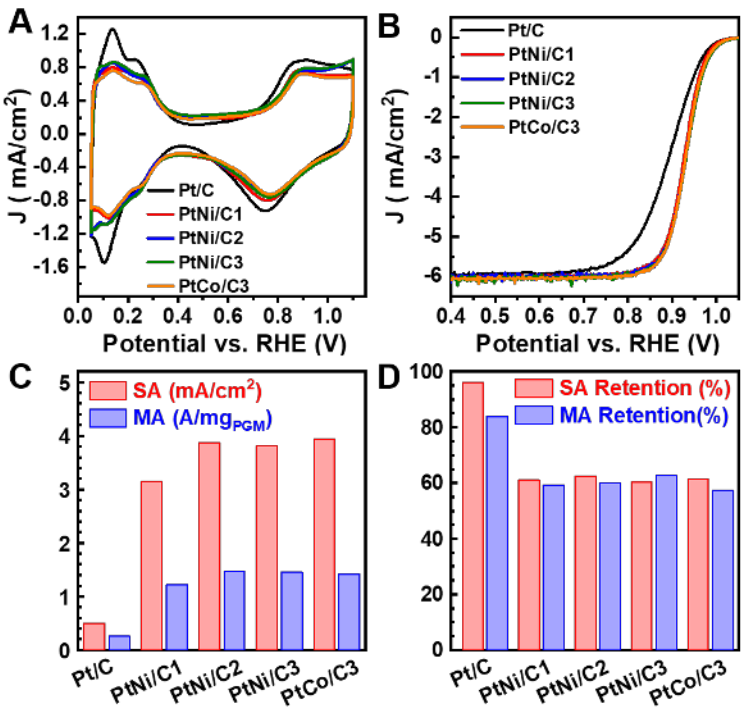

Fig. S6. Rotating disk electrode (RDE) test of catalysts. **(A)** cyclic voltammetry curves of tested in N_2 saturated 0.1 M $HClO_4$. **(B)** ORR polarization curves in O_2 saturated 0.1 M $HClO_4$ (1600 rpm). **(C)** comparison mass activities (MA) and specific activities (SA). **(D)** comparison of retention ratios of mass activities.

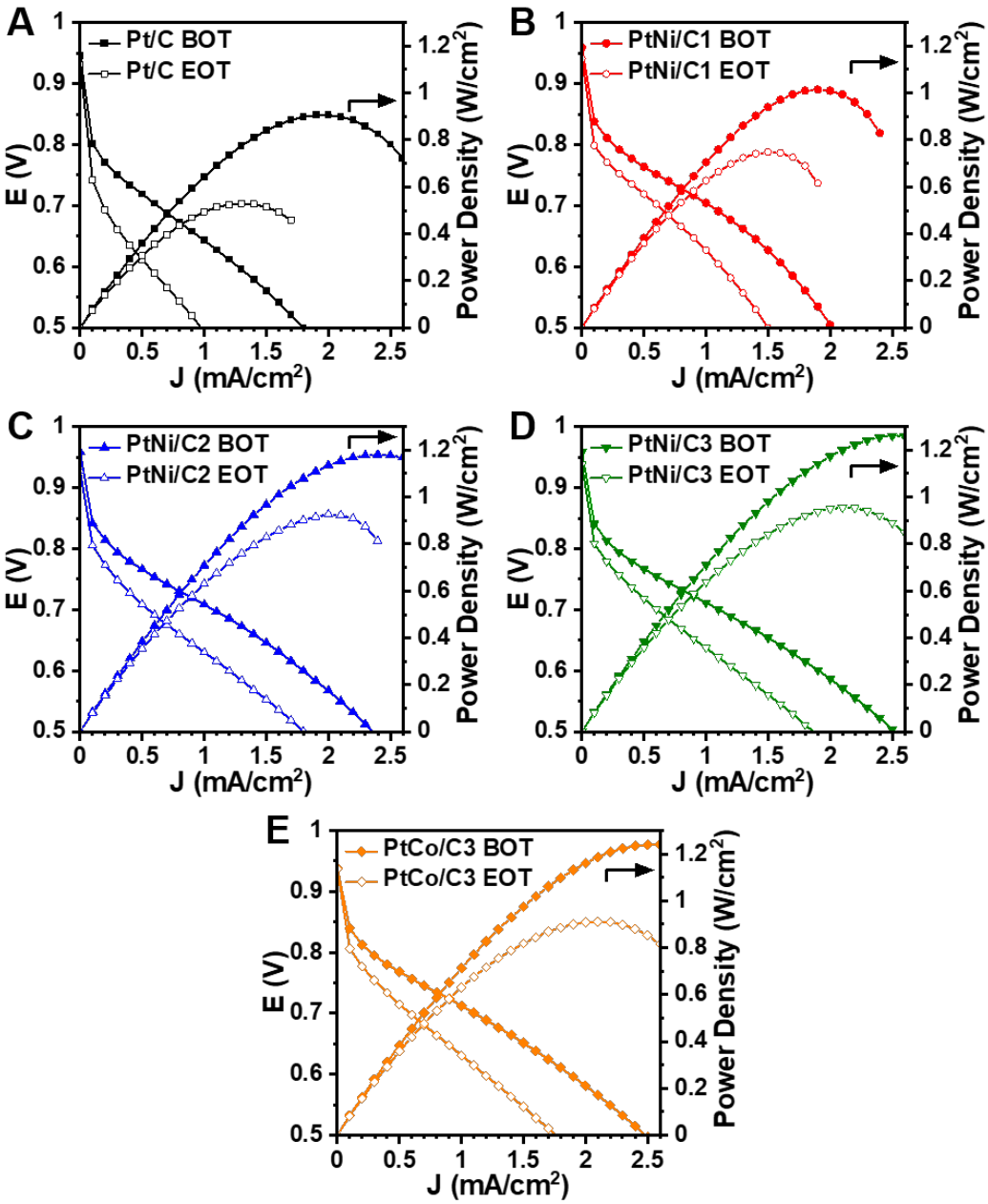

Fig. S7. Comparison of MEAs at BOT and EOT in H_2/Air test. (A) Pt/C, (B) PtNi/C, (C) PtNi/C2, (D) PtNi/C3, (E) PtCo/C3. Testing condition is 80°C, 150 kPa_{abs}.

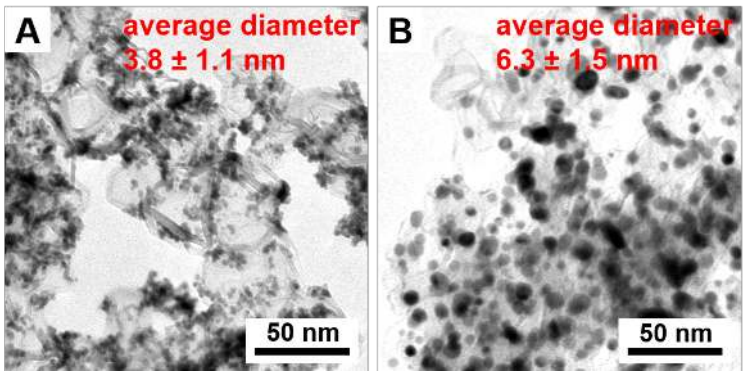

Fig. S8. TEM images of commercial Pt/C catalyst: (A) before MEA test, **(B)** after 30k square wave cycles in the MEA test.

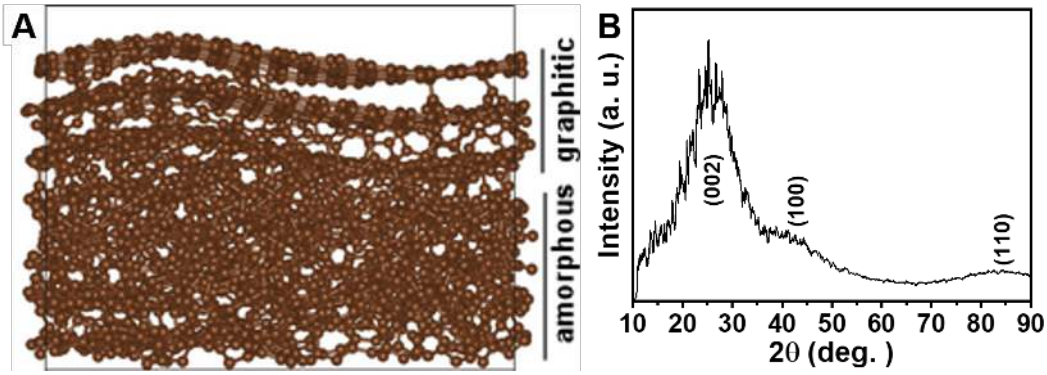

Fig. S9. Predicted Core-shell like carbon substrate structure with its predicted XRD pattern. **(A)** The predicted carbon substrate has a structure similar to that obtained by experimentally. It consists of three layers of graphitic carbon on top of amorphous carbon on the bottom. We heated the amorphous carbon to 6000 K and quenched to 300 K, followed by heating to 3500 K temperature followed by quenching at 300 K at 100 K/ps rate. The final carbon density in our structure is 2.15 g/cm^3. **(B)** The predicted X-ray diffraction pattern (XRD), which is similar to experimental data as shown in **Fig. S2B**. The XRD used Cu source radiation with powder diffraction technique at 0.05 step size.

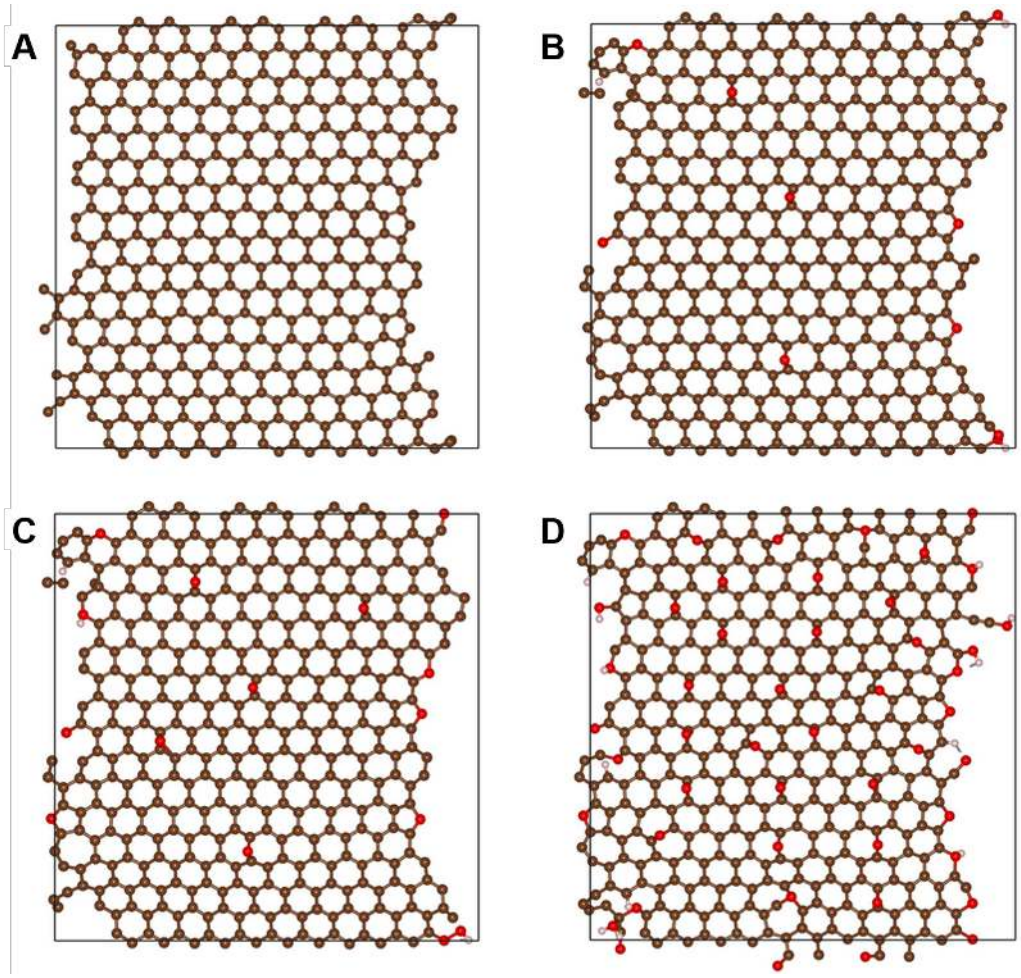

Fig. S10. The carbon surface oxidation patterns used in the MD simulations. (**A)** Pure graphitic surface (0% oxygen). **(B), (C),** and **(D)** are 2.5%, 4.0% and 12.0% oxygen to carbon ratios. All structures were minimized and equilibrated for 100 ps at 300K temperature and 0.2 fs time step. (coffee: carbon, red: oxygen, off-white: hydrogen).

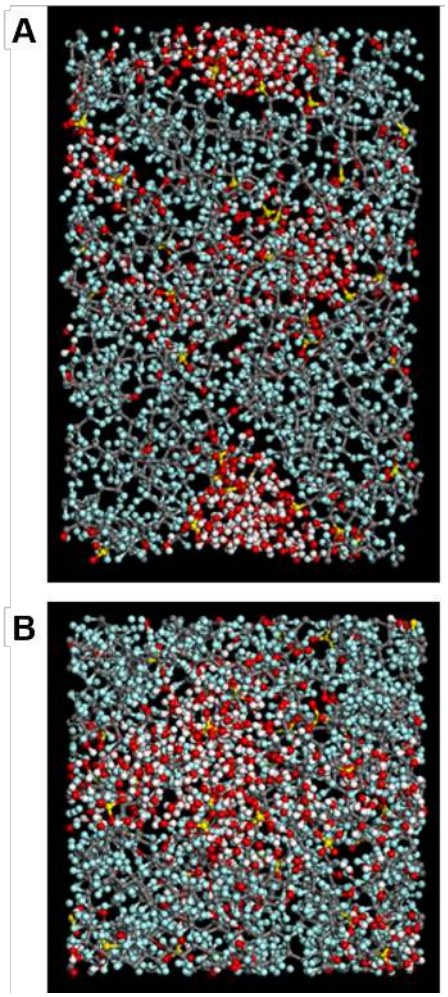

Fig. S11. Predicted structures from ReaxFF MD. The Hydrated PFSA ionomer structure contains non-polar hydrophobic parts (polytetrafluoroethylene [PTFE] backbone) and hydrophilic sulfonic acid (-SO_3^-) parts. **(A)** The side view of PFSA ionomer molecules with a cluster of waters (12 H_2O/-SO_3^-) at the carbon ionomer interface. **(B)** The top view of the panel **(A)**. The structures were equilibrated at 600 K for 200 ps and cooled down to 300 K at 0.2 fs time step (gray: carbon; light cyan: Florine; red: oxygen; white: hydrogen; yellow: sulfur).

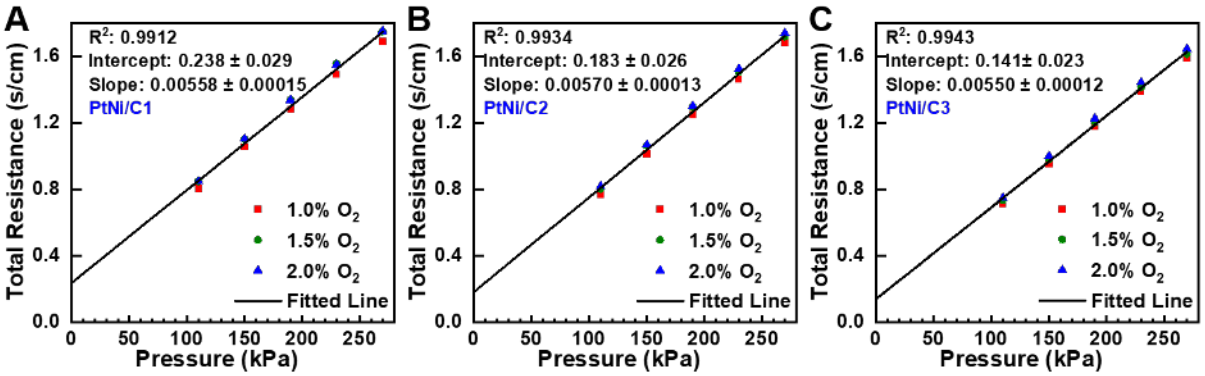

Fig. S12. The measured total oxygen transport resistances in MEAs plotted with the total pressure during the measurement: (**A)** PtNi/C1, **(B)** PtNi/C2, **(C)** PtNi/C3. The total oxygen transport resistance can be separated into pressure dependent part ($R^{P\text{-}d}$) and pressure independent part ($R^{P\text{-}ind}$), which represents the Knudsen diffusion and diffusion of oxygen through the ionomer layer in the catalyst layer[52,53]. Thus, the pressure independent part is critical for oxygen transport in an operating fuel cell. The relationship of total oxygen resistance (R_{total}), pressure dependent part of oxygen transport resistance ($R^{P\text{-}d}$), and pressure independent part of oxygen transport resistance ($R^{P\text{-}ind}$) can be expressed in the following Eq. S1 (noted in the Method part "Oxygen Transport Resistance Test for MEA").

$$R_{total} = R^{P-d} + R^{P-ind} \qquad \text{Eq. S1}$$

Table S1. BET surface area and XRD interlayer distance of carbon materials.

Sample	BET surface area (m^2/g)	XRD interlayer distance (nm)
C1	766	0.355
C2	761	0.355
C3	755	0.355

Table S2. EDS composition analysis of catalysts before the MEA test and at the end of test (EOT) (after 30000 square wave ADT cycles in MEA test).

	Atomic Ratio (%)		
	Pt	Ni	Co
PtNi/C1	71.9	28.1	/
PtNi/C2	73.3	26.7	/
PtNi/C3	74.2	25.8	/
PtCo/C3	82.1	/	17.9
PtNi/C1 MEA EOT	88.8	11.2	/
PtNi/C2 MEA EOT	89.2	10.8	/
PtNi/C3 MEA EOT	89.6	10.4	/
PtCo/C3 MEA EOT	89.3	/	10.7

Table S3. Specific activity (SA), mass activity (MA), and electrochemical active surface area ECSA comparison of catalysts based on RDE test results.

	SA (mA/cm^2)	MA (A/mg_{PGM})	ECSA (m^2/g_{PGM})
Pt/C	0.50	0.26	52.0
PtNi/C1	3.15	1.22	38.7
PtNi/C2	3.87	1.47	38.0
PtNi/C3	3.81	1.45	38.1
PtCo/C3	3.94	1.42	36.0

Table S4. Comparison of roughness factor for prepared MEAs.

MEA	Roughness Fatcor (cm^2/cm^2_{Geo})
Pt/C	41.7
PtNi/C1	36.3
PtNi/C2	37.6
PtNi/C3	38.5
PtCo/C3	39.6

Table S5. Comparison of the mass activity of tested catalysts and several representative catalysts reported in recent literature. The comparison includes the mass activity at the beginning of test (BOT, before ADT), the mass activity at the EOT, which is after ADT cycles, the MA retention ratio, ADT cycle protocol, and the cathode PGM loading.

Catalyst	Cathode Loading (mg_{PGM}/cm^2)	Mass Activity (A/mg_{PGM})		Mass Activity Retention	ADT cycle number	ADT test condition	Reference
		BOT	EOT				
DOE Target	⩽0.1	>0.44	>0.264	>60%	30000	**square wave#**	Ref.[5,35]
Pt/C	0.10	0.32	0.11	33%	30000	**square wave**	this work
PtNi/C3	0.10	0.65	0.42	65%	30000	**square wave**	this work
PtCo/C3	0.10	0.72	0.44	61%	30000	**square wave**	this work
PtNi (P2-SA)	0.1	0.64*	0.52*	81%	30000	Triangle wave	Ref.[14]
Pt ML/Pd	0.134	0.17	0.11*	65%	20000	Triangle wave	Ref. [56]
D-PtCo	0.2	0.490	0.330	67.3%	30000	Triangle wave	Ref.[15]
$L1_0$-FePt	0.103	0.210	0.230	109.5%	30000	Trapezoidal Wave	Ref.[16]
$L1_0$-CoPt	0.105	0.560	0.450	80.4%	30000	Trapezoidal Wave	Ref.[17]

*Data extracted from plots.

The square wave ADT represents the newly suggested protocols for long term durability evaluation [35,36], and has five times acceleration than the typical triangle wave ADT protocol used previously [36].

Table S6. Rated power reported in representative literature. Measurements are performed at 250 kPa_{abs}, 94 ºC.

Catalyst	Rated Power (W/cm^2)		Loss in Voltage at 0.8 A/cm^2 (mV)	Reference
	BOT	EOT		
DOE Target	> 1.00		< 30.0	Ref.[35]
PtCo/HSC-e	1.21	NA	NA	Ref.[18]
PtCo/HSC-f	1.26	NA	NA	Ref.[18]
PtNi/C3	1.21	1.05	16.2	this work
PtCo/C3	1.16	1.03	16.9	this work

NA: not available

Table S7. Interface energy predicted from ReaxFF MD for the hydrated PFSA ionomer on different carbon surfaces. (12 H_2O/-SO_3^- at the interface, Fig. 4).

Percentage (%) of Surface Oxygen	Interface Energy (kcal/Å^2)
0	-48.17
2.5	-50.69
4.0	-50.54
12.0	-48.53

Reference:

1 Weydahl, H., Gilljam, M., Lian, T., Johannessen, T. C., Holm, S. I. & Hasvold, J. Ø. (2019). Fuel cell systems for long-endurance autonomous underwater vehicles – challenges and benefits. Int. J. Hydrogen Energy,

2 Ustolin, F. & Taccani, R. (2018). Fuel cells for airborne usage: Energy storage comparison. Int. J. Hydrogen Energy 43, 11853-11861.

3 Debe, M. K. (2012). Electrocatalyst approaches and challenges for automotive fuel cells. Nature 486, 43.

4 Kongkanand, A., Gu, W. & Mathias, M. F.(2017). in *Encyclopedia of Sustainability Science and Technology* (ed Robert A. Meyers) 1-20 (Springer New York).

5 Kongkanand, A. & Mathias, M. F. (2016). The Priority and Challenge of High-Power Performance of Low-Platinum Proton-Exchange Membrane Fuel Cells. J. Phys. Chem. Lett. 7, 1127-1137.

6 Seh, Z. W., Kibsgaard, J., Dickens, C. F., Chorkendorff, I., Nørskov, J. K. & Jaramillo, T. F. (2017). Combining theory and experiment in electrocatalysis: Insights into materials design. Science 355, eaad4998.

7 Pedersen, C. M., Escudero-Escribano, M., Velázquez-Palenzuela, A., Christensen, L. H., Chorkendorff, I. & Stephens, I. E. L. (2015). Benchmarking Pt-based electrocatalysts for low temperature fuel cell reactions with the rotating disk electrode: oxygen reduction and hydrogen oxidation in the presence of CO (review article). Electrochim. Acta 179, 647-657.

8 Xie, C., Niu, Z., Kim, D., Li, M. & Yang, P. (2020). Surface and Interface Control in Nanoparticle Catalysis. Chem. Rev. 120, 1184-1249.

9 Jacob, T. & Goddard III, W. A. (2006). Water Formation on Pt and Pt-based Alloys: A Theoretical Description of a Catalytic Reaction. ChemPhysChem 7, 992-1005.

10 Zhang, Z., Luo, Z., Chen, B., Wei, C., Zhao, J., Chen, J., Zhang, X., Lai, Z., Fan, Z., Tan, C. *et al.* (2016). One-Pot Synthesis of Highly Anisotropic Five-Fold-Twinned PtCu Nanoframes Used as a

Bifunctional Electrocatalyst for Oxygen Reduction and Methanol Oxidation. Adv. Mater. 28, 8712-8717.

11 Holdcroft, S. (2014). Fuel Cell Catalyst Layers: A Polymer Science Perspective. Chem. Mater. 26, 381-393.

12 Weber, A. Z. & Kusoglu, A. (2014). Unexplained transport resistances for low-loaded fuel-cell catalyst layers. J. Mater. Chem. A 2, 17207-17211.

13 Li, W., Chen, Z., Xu, L. & Yan, Y. (2010). A solution-phase synthesis method to highly active Pt-Co/C electrocatalysts for proton exchange membrane fuel cell. J. Power Sources 195, 2534-2540.

14 Han, B., Carlton, C. E., Kongkanand, A., Kukreja, R. S., Theobald, B. R., Gan, L., O'Malley, R., Strasser, P., Wagner, F. T. & Shao-Horn, Y. (2015). Record activity and stability of dealloyed bimetallic catalysts for proton exchange membrane fuel cells. Energy Environ. Sci. 8, 258-266.

15 Jia, Q., Caldwell, K., Strickland, K., Ziegelbauer, J. M., Liu, Z., Yu, Z., Ramaker, D. E. & Mukerjee, S. (2015). Improved Oxygen Reduction Activity and Durability of Dealloyed PtCox Catalysts for Proton Exchange Membrane Fuel Cells: Strain, Ligand, and Particle Size Effects. ACS Catal. 5, 176-186.

16 Li, J., Xi, Z., Pan, Y.-T., Spendelow, J. S., Duchesne, P. N., Su, D., Li, Q., Yu, C., Yin, Z., Shen, B. *et al.* (2018). Fe Stabilization by Intermetallic L10-FePt and Pt Catalysis Enhancement in L10-FePt/Pt Nanoparticles for Efficient Oxygen Reduction Reaction in Fuel Cells. J. Am. Chem. Soc. 140, 2926-2932.

17 Li, J., Sharma, S., Liu, X., Pan, Y.-T., Spendelow, J. S., Chi, M., Jia, Y., Zhang, P., Cullen, D. A., Xi, Z. *et al.* (2019). Hard-Magnet L10-CoPt Nanoparticles Advance Fuel Cell Catalysis. Joule 3, 124-135.

18 Yarlagadda, V., Carpenter, M. K., Moylan, T. E., Kukreja, R. S., Koestner, R., Gu, W., Thompson, L. & Kongkanand, A. (2018). Boosting Fuel Cell Performance with Accessible Carbon Mesopores. ACS Energy. Lett. 3, 618-621.

19 Inoue, G. & Kawase, M. (2016). Effect of porous structure of catalyst layer on effective oxygen diffusion coefficient in polymer electrolyte fuel cell. J. Power Sources 327, 1-10.

20 Nonoyama, N., Okazaki, S., Weber, A. Z., Ikogi, Y. & Yoshida, T. (2011). Analysis of Oxygen-Transport Diffusion Resistance in Proton-Exchange-Membrane Fuel Cells. J. Electrochem. Soc. 158, B416-B423.

21 Kreuer, K. D., Schuster, M., Obliers, B., Diat, O., Traub, U., Fuchs, A., Klock, U., Paddison, S. J. & Maier, J. (2008). Short-side-chain proton conducting perfluorosulfonic acid ionomers: Why they perform better in PEM fuel cells. J. Power Sources 178, 499-509.

22 Yu, H., Roller, J. M., Mustain, W. E. & Maric, R. (2015). Influence of the ionomer/carbon ratio for low-Pt loading catalyst layer prepared by reactive spray deposition technology. J. Power Sources 283, 84-94.

23 Li, H., Tang, Y., Wang, Z., Shi, Z., Wu, S., Song, D., Zhang, J., Fatih, K., Zhang, J., Wang, H. *et al.* (2008). A review of water flooding issues in the proton exchange membrane fuel cell. J. Power Sources 178, 103-117.

24 Orfanidi, A., Madkikar, P., El-Sayed, H. A., Harzer, G. S., Kratky, T. & Gasteiger, H. A. (2017). The Key to High Performance Low Pt Loaded Electrodes. J. Electrochem. Soc. 164, F418-F426.

25 Ott, S., Orfanidi, A., Schmies, H., Anke, B., Nong, H. N., Hübner, J., Gernert, U., Gliech, M., Lerch, M. & Strasser, P. (2019). Ionomer distribution control in porous carbon-supported catalyst layers for high-power and low Pt-loaded proton exchange membrane fuel cells. Nat. Mater. 19, 77-85.

26 Jang, S. S., Molinero, V., Çağın, T. & Goddard, W. A. (2004). Nanophase-Segregation and Transport in Nafion 117 from Molecular Dynamics Simulations: Effect of Monomeric Sequence. J. Phys. Chem. B 108, 3149-3157.

27 Sha, Y., Yu, T. H., Merinov, B. V., Shirvanian, P. & Goddard, W. A. (2011). Oxygen Hydration Mechanism for the Oxygen Reduction Reaction at Pt and Pd Fuel Cell Catalysts. J. Phys. Chem. Lett. 2, 572-576.

28 Zhang, L., Ji, L., Glans, P.-A., Zhang, Y., Zhu, J. & Guo, J. (2012). Electronic structure and chemical bonding of a graphene oxide–sulfur nanocomposite for use in superior performance lithium–sulfur cells. Phys. Chem. Chem. Phys. 14, 13670-13675.

29 Banerjee, S., Hemraj-Benny, T., Balasubramanian, M., Fischer, D. A., Misewich, J. A. & Wong, S. S. (2004). Ozonized single-walled carbon nanotubes investigated using NEXAFS spectroscopy. Chem. Commun., 772-773.

30 Banerjee, S., Hemraj-Benny, T., Balasubramanian, M., Fischer, D. A., Misewich, J. A. & Wong, S. S. (2004). Surface Chemistry and Structure of Purified, Ozonized, Multiwalled Carbon Nanotubes Probed by NEXAFS and Vibrational Spectroscopies. ChemPhysChem 5, 1416-1422.

31 Wang, W., Ruiz, I., Lee, I., Zaera, F., Ozkan, M. & Ozkan, C. S. (2015). Improved functionality of graphene and carbon nanotube hybrid foam architecture by UV-ozone treatment. Nanoscale 7, 7045-7050.

32 O'Reilly, J. M. & Mosher, R. A. (1983). Functional groups in carbon black by FTIR spectroscopy. Carbon 21, 47-51.

33 Prest, W. M. & Mosher, R. A.(1982). in *Colloids and Surfaces in Reprographic Technology* Vol. 200 *ACS Symposium Series* Ch. 11, 225-247 (AMERICAN CHEMICAL SOCIETY).

34 Powell, C. J. & Jablonski, A.(2010). NIST Electron Inelastic-Mean-Free-Path Database - Version 1.2. (National Institute of Standards and Technology).

35 *Fuel Cell Technologies Office Multi-Year Research, Development, and Demonstration Plan*, <https://www.energy.gov/eere/fuelcells/downloads/fuel-cell-technologies-office-multi-year-research-development-and-22> (2017).

36 Stariha, S., Macauley, N., Sneed, B. T., Langlois, D., More, K. L., Mukundan, R. & Borup, R. L. (2018). Recent Advances in Catalyst Accelerated Stress Tests for Polymer Electrolyte Membrane Fuel Cells. J. Electrochem. Soc. 165, F492-F501.

37 Borup, R. L., Kusoglu, A., Neyerlin, K. C., Mukundan, R., Ahluwalia, R. K., Cullen, D. A., More, K. L., Weber, A. Z. & Myers, D. J. (2020). Recent developments in catalyst-related PEM fuel cell durability. Current Opinion in Electrochemistry 21, 192-200.

38 *DOE Technical Targets for Polymer Electrolyte Membrane Fuel Cell Components*, <https://energy.gov/eere/fuelcells/doe-technical-targets-polymer-electrolyte-membrane-fuel-cell-components> (2016).

39 Zhao, Z., Chen, C., Liu, Z., Huang, J., Wu, M., Liu, H., Li, Y. & Huang, Y. (2019). Pt-Based Nanocrystal for Electrocatalytic Oxygen Reduction. Adv. Mater. 31, 1808115.

40 Yoshida, T. & Kojima, K. (2015). Toyota MIRAI Fuel Cell Vehicle and Progress Toward a Future Hydrogen Society. Electrochem. Soc. Interface. 24, 45-49.

41 Ozden, A., Shahgaldi, S., Li, X. & Hamdullahpur, F. (2019). A review of gas diffusion layers for proton exchange membrane fuel cells—With a focus on characteristics, characterization techniques, materials and designs. Prog. Energy Combust. Sci. 74, 50-102.

42 Kusoglu, A. & Weber, A. Z. (2017). New Insights into Perfluorinated Sulfonic-Acid Ionomers. Chem. Rev. 117, 987-1104.

43 Kienitz, B., Kolde, J., Priester, S., Baczkowski, C. & Crum, M. (2011). Ultra-Thin Reinforced Ionomer Membranes to Meet Next Generation Fuel Cell Targets. ECS Trans. 41, 1521-1530.

44 Cao, L., Zhao, Z., Liu, Z., Gao, W., Dai, S., Gha, J., Xue, W., Sun, H., Duan, X., Pan, X. *et al.* (2019). Differential Surface Elemental Distribution Leads to Significantly Enhanced Stability of PtNi-Based ORR Catalysts. Matter 1, 1567-1580.

45 Sulek, M., Adams, J., Kaberline, S., Ricketts, M. & Waldecker, J. R. (2011). In situ metal ion contamination and the effects on proton exchange membrane fuel cell performance. J. Power Sources 196, 8967-8972.

46 G. A. Melo, L., Hitchcock, A. P., Jankovic, J., Stumper, J., Susac, D. & Berejnov, V. (2017). Quantitative Mapping of Ionomer in Catalyst Layers by Electron and X-ray Spectromicroscopy. ECS Trans. 80, 275-282.

47 Cullen, D. A., Koestner, R., Kukreja, R. S., Liu, Z. Y., Minko, S., Trotsenko, O., Tokarev, A., Guetaz, L., Meyer, H. M., Parish, C. M. *et al.* (2014). Imaging and Microanalysis of Thin Ionomer Layers by Scanning Transmission Electron Microscopy. J. Electrochem. Soc. 161, F1111-F1117.

48 Wu, J., Zhu, X., West, M. M., Tyliszczak, T., Shiu, H.-W., Shapiro, D., Berejnov, V., Susac, D., Stumper, J. & Hitchcock, A. P. (2018). High-Resolution Imaging of Polymer Electrolyte Membrane Fuel Cell Cathode Layers by Soft X-ray Spectro-Ptychography. J. Phys. Chem. C 122, 11709-11719.

49 Soboleva, T., Zhao, X., Malek, K., Xie, Z., Navessin, T. & Holdcroft, S. (2010). On the Micro-, Meso-, and Macroporous Structures of Polymer Electrolyte Membrane Fuel Cell Catalyst Layers. ACS Appl. Mater. Interfaces 2, 375-384.

50 Yu, P. T., Gu, W., Makharia, R., Wagner, F. T. & Gasteiger, H. A. (2006). The Impact of Carbon Stability on PEM Fuel Cell Startup and Shutdown Voltage Degradation. ECS Trans. 3, 797-809.

51 Goddard, W., Merinov, B., van Duin, A., Jacob, T., Blanco, M., Molinero, V., Jang, S. S. & Jang, Y. H. (2006). Multi-paradigm multi-scale simulations for fuel cell catalysts and membranes. Mol. Simulat. 32, 251-268.

52 Baker, D. R., Caulk, D. A., Neyerlin, K. C. & Murphy, M. W. (2009). Measurement of Oxygen Transport Resistance in PEM Fuel Cells by Limiting Current Methods. J. Electrochem. Soc. 156, B991-B1003.

53 Garsany, Y., Atkinson, R. W., Gould, B. D. & Swider-Lyons, K. E. (2018). High power, Low-Pt membrane electrode assemblies for proton exchange membrane fuel cells. J. Power Sources 408, 38-45.

54 van Duin, A. C. T., Dasgupta, S., Lorant, F. & Goddard, W. A. (2001). ReaxFF: A Reactive Force Field for Hydrocarbons. J. Phys. Chem. A 105, 9396-9409.

55 Plimpton, S. (1995). Fast Parallel Algorithms for Short-Range Molecular Dynamics. J. Comput. Phys. 117, 1-19.

56 Kongkanand, A., Subramanian, N. P., Yu, Y., Liu, Z., Igarashi, H. & Muller, D. A. (2016). Achieving High-Power PEM Fuel Cell Performance with an Ultralow-Pt-Content Core–Shell Catalyst. ACS Catal. 6, 1578-1583.